University of Pennsylvania
ScholarlyCommons

Departmental Papers (ESE) | Department of Electrical & Systems Engineering

7-1-2007

Visual Servoing for Nonholonomically Constrained Three Degree of Freedom Kinematic Systems

Gabriel A.D. Lopes
University of Pennsylvania

Daniel E. Koditschek
University of Pennsylvania, kod@seas.upenn.edu

Postprint version. Published in *International Journal of Robotics Research*, Volume 26, Issue 7, July 2007, pages 715-736.
Publisher URL: http://dx.doi.org/10.1177/0278364907080737

This paper is posted at ScholarlyCommons. http://repository.upenn.edu/ese_papers/428
For more information, please contact repository@pobox.upenn.edu.

Visual Servoing for Nonholonomically Constrained Three Degree of Freedom Kinematic Systems

Gabriel A. D. Lopes, *Student Member, IEEE* and Daniel E. Koditschek, *Fellow, IEEE*

***Abstract*— This paper addresses problems of robot navigation with nonholonomic motion constraints and perceptual cues arising from onboard visual servoing in partially engineered environments. We propose a general hybrid procedure that adapts to the constrained motion setting the standard feedback controller arising from a navigation function in the fully actuated case. This is accomplished by switching back and forth between moving "down" and "across" the associated gradient field toward the stable manifold it induces in the constrained dynamics. Guaranteed to avoid obstacles in all cases, we provide conditions under which the new procedure brings initial configurations to within an arbitrarily small neighborhood of the goal.**

We summarize simulation results on a sample of visual servoing problems with a few different perceptual models. We document the empirical effectiveness of the proposed algorithm by reporting the results of its application to outdoor autonomous visual registration experiments with the robot RHex guided by engineered beacons.

***Index Terms*— Visual servoing, level sets, robotics, nonholonomic, navigation.**

I. Introduction

In this paper we introduce a robust feedback controller for outdoor navigation of a legged robot guided only by visual cues. Conceptually, there are three broad problems associated with this task. First, the requirement for perceptually reliable landmarks is an instance of the long-standing "early vision" problem that we explicitly avoid by engineering the visual beacons that comprise the physical landmarks. Second, the transformation of discrepancies between perceived and desired visual landmark appearance into feedback forces. These must be capable of "safely" correcting the errors in pose that cause them, effected by a monocular camera via a slightly generalized extension of prior work. Finally, the effective application of these restoring forces in a manner that respects both the constrained control authority over rigid body motion afforded by a legged gait as well as the perceptual requirements represents our central contribution.

We pursue a solution linking the second and third problems by encoding the perceived discrepancies in terms of artificial potential functions. For fully actuated systems, potential-dissipative force fields offer a natural and direct generalization of linear proportional-derivative servo control for general mechanical systems [1]. The wide popularity of such PD controllers attests to their robustness against sensor noise and imperfect models. However, for underactuated systems when the number of independently actuated degrees of freedom decreases relative to the dimension of the total configuration space, there is no general method for applying PD control. For autonomous outdoor robots, it is crucial to develop perception-driven controllers, yet in consequence of ubiquitous power-to-weight limitations, autonomous robots are intrinsically underactuated. Hence, we draw the greatest practical motivation for extending PD methods to underactuated settings precisely in such contexts as visual servoing for a rugged and underactuated outdoor vehicle like the hexapod, RHex [2].

This paper presents an extension of PD control to the class of two-actuator, three-degree-of-freedom mechanical systems that includes the simple "unicycle" kinematics crudely descriptive of the horizontal plane behavior of RHex. By so modeling the robot as a drift-free constrained kinematic system and by treating the perceptual limitations of a monocular camera observing the robot's horizontal plane pose as incurring obstacles in the robot's configuration space, we arrive at the formal problem of set point regulation in the face of simultaneously nonholonomic motion constraints and holonomic perception constraints.[1]

A. Relevant Literature

A growing robotics literature treats visual sensory perceptual limitations as effectively introducing (holonomic) obstacles in a robot's configuration space. Ostrowsky [4] uses a blimp equipped with a camera, maintaining a ball on the center of the camera's field of view (FOV). Chaumette [5]–[7], Hirzinger [8] and Chesi [9] position fully actuated camera arms in relation to a collection of features, always making sure that they stay in the FOV. In [5], [6] and [9] self-occlusions are dealt explicitly by the controller while in [7] and [8] virtual 3D models are fitted to the image, allowing for temporary self-occlusions. Cowan [10] and Chen [11] use navigation functions [12] to position a 6dof arm, again keeping the features in the FOV and accounting for self-occlusions. Mansard [13] uses a sequence of tasks that constrain or release

Manuscript received November 2nd, 2005; revised August 24th, 2006 and accepted November 24th, 2006. This work was supported by The University of Michigan, by DARPA/ONR N00014-98-1-0747, by DARPA/SPAWAR N660011-03-C-8045 and by Fundação para a Ciência e Tecnologia - Portugal, with the fellowship PRAXIS XXI/BD/18148/98. This work was presented in part at IEEE/RSJ International Conference on Intelligent Robots and Systems, Sendai, Japan, September 28 - October 2, 2004.

G. Lopes is with University of Michigan, currently a visiting student at the University of Pennsylvania, 200 S. 33rd St., Philadelphia, PA 19104, USA, Tel +1-215-898-9241, Fax +1-215-573-2068 (e-mail: glopes@umich.edu)

D. Koditschek is with the Electrical & Systems Engineering, University of Pennsylvania (e-mail: kod@ese.upenn.edu)

[1]Note that, in general, PD controllers lift very naturally to the dynamical setting as well. See reference [3] for a sketch of the theoretical steps required to lift the algorithm proposed in this paper to a second order version of the quasi-static model considered here.

particular degrees of freedom of an holonomically constrained arm, mixing together constraints arising from joint limits, occlusions and obstacle avoidance simultaneously.

There is a considerably older literature focused on the control of nonholonomically constrained mechanical systems. Brockett's classical result [14] establishes that nonholonomically constrained systems cannot be stabilized by smooth, time-invariant feedback. In general, applying a smooth time-invariant feedback control law to such a system produces an attracting center manifold in the configuration space. The goal lies on the center manifold and attracts all initial conditions on its (generically transverse) co-dimension one stable manifold (a leaf of the foliation [15] generated by the constraints). Almost all of this literature assumes an unbounded and obstacle-free (simply connected) configuration space. In order to stabilize at a particular goal, Khennouf [16] and Luo [17] use invariant manifolds; Astlofi [18], makes the system discontinuous and stabilizes it by continuous feedback control; Tayebi [19] use back stepping design; Monaco [20] apply multi-rate digital control; Sordalen [21], Pomet [22] and Samson [23] propose time varying feedback control laws; Gans [24] uses hybrid controllers; Morin and Samson [25] apply the concept of transverse vector fields and Bloch [26] develops reduced-order state equations for feedback control.

In prior literature on nonholonomic feedback control most closely related to our approach, Ikeda et al. [27] introduce the notion of Variable Constraint Control (VCC) designed to achieve an invariant manifold that goes through the goal, in effect, picking out a distinguished trajectory lying within the goals stable manifold. The formulation results in a procedure that achieves the point goal in two steps, but is not designed with the consideration of obstacles in mind. In our work, each different class of obstacles, once encoded by the appropriate gradient field, gives rise to a different stable manifold, and we cannot assume that it will be easy find that surface (much less any particular trajectory within it) leading us to study the iterative application of a controller which repeatedly targets an approximation to it.

More recently Murrieri [28], Folio [29], Kantor [30] and Bhattacharya [31] have combined both motion constraints and perceptual limitations. However, in general, these authors assume a particular set of constraints for which a feedback control law is subsequently developed taking into account the special form. Murrieri et al. develops a collection of specialized Lyapunov based controllers for a wheeled vehicle, with perception limited by the monocular camera's field of view. Folio et al. proposes switching between three controllers that either deal with the visual servoing task at hand, beacon occlusion or obstacle avoidance. However their task is facilitated by a pan camera mechanism on a cart like car, resulting in the problem of stabilization in $\mathsf{SE}(2)$ with 3 available inputs. Kantor et al. combine Ikeda's VCC with the notion of sequential composition of controllers [32] to drive the robot RHex to a specified goal location. This approach can result in optimized trajectories but can be hard to reuse on systems with different motion models and/or different perceptual constraints. Bhattacharya et al. take a geometric approach and find minimum length paths.

B. Contributions of this paper

In this paper, we take a few steps toward a more general approach to perception-based servoing that decouples the (typically holonomic) perceptual constraints from the (typically nonholonomic) kinematic constraints by adapting an "arbitrary" navigation function [12] to an "arbitrary" nonholonomically constrained first order mechanism operating in the configuration space comprising the navigation function's domain. The encoding of holonomic constraints via navigation functions is a very effective mean of constructing "designer" basins around specified goal points for fully actuated first and second order mechanisms. For example, in visual servoing applications, the navigation function takes into account external constraints like limited field of view, obstacles and so on. We are most immediately motivated by the prospect of extending Cowan's [10] work on navigation with triple-beacon landmarks to the robot RHex. However, we will introduce a more general framework for nonholonomically constrained visual servoing via PD control and offer two other examples of navigation functions arising from perceptual apparatus to give some feeling for the virtue of the more general view.

The paper makes three specific contributions. First, we adapt Cowan's [10] construction of a navigation function for moving landmarks viewed by a stationary monocular camera to the "inside out" case of a moving monocular camera viewing a fixed landmark. This entails generalizing the "camera map" for convex landmarks to the more general setting relevant to outdoor mobile robotics with landmarks formed by any triple of beacons in general position (i.e., whose convex hull encloses a set with non-empty interior on $\mathsf{SE}(2)$).

Second, we construct a hybrid controller for arbitrary navigation functions applied to arbitrary drift-free three dimensional control systems with two independent control inputs. The resulting switching feedback law guarantees "practical stability" (in the sense of Morin and Samson [25]: convergence to an arbitrarily small specified neighborhood of the goal) with the added guarantee that no obstacle will ever be encountered along the way. We offer very general (and easily verified) sufficient conditions under which the basin (the set of initial configurations brought into the goal's small neighborhood) includes a far larger "local surround" bounded by the "highest" level set of the navigation function that is still a topological sphere. We present additional "global" conditions (albeit much more narrowly adapted to the specific examples at hand) sufficient to guarantee that the basin includes all initial conditions except possibly a set of measure zero[2] .

Third, we implement an instance of this visual servoing framework on the robot RHex [2] in general outdoor terrain viewing through a monocular camera landmarks comprised of three beacons in arbitrary general position. We provide extensive experimental data to document the robustness of the

[2]In general, there is no guarantee that these conditions will prevail, and we can make no general statements about the global versions of this problem. However, one of the central motivations for embracing navigation functions and their associated controllers is the possibility of developing still more abstracted compositions using suitably arranged "deployments" of their computable basins, such as the "back-chaining" sequential composition in [32].

algorithm against the inaccuracies in the (very crude) control model and the many practical sources of noise in the sensor suite's acquisition of the naturally illuminated outdoor scene.

C. Organization of this Paper

We present the ingredients of the specific RHex servoing problem in Section II, introducing the camera map arising from a monocular camera's view of a three-beacon landmark, the navigation function associated with it, and a very simple (and only loosely accurate) motion control model for RHex's horizontal plane behavior. We introduce the hybrid controller along with a number of preliminary technical developments before presenting our general mathematical result in Section III. Namely, we lay out the hybrid algorithm, state the sufficient conditions for convergence from the "local surround" and provide more specific sufficient conditions for essential global convergence at the price of less general assumptions appropriate to the particular case — necessarily so, because a "general extension" would include a constructive solution of the global navigation problem which we are far from claiming to encompass within the scope of this work. Finally, in Section IV we apply the foregoing constructions to the central motivation for this paper: the specific case of a visual servo algorithm for the robot RHex. We present statistics documenting the successful outdoor implementation in the final portion of Section IV, and close with brief concluding remarks in Section V.

II. A Visual servoing problem

There are three central ingredients to formulating the problem at hand. First, we introduce the perceptual model relating a parametrized family of visual landmarks to the resulting family of "camera maps" that associate an observer's rigid body configuration with the state of its visual sensor. Next, we construct a potential function built upon that perceptual model whose gradient field would be capable of guiding a fully actuated robot to an arbitrarily specified visual sensor state (and hence a unique rigid pose) without ever losing sight of the landmark along the way. Finally, we review the simple "unicycle" motion model — a familiar nonholonomically constrained mechanical system that captures the essential limitations of our robot's control authority respecting its horizontal plane behavior — limitations that preclude successful application of the proposed gradient field. The visual servoing problem solved by this paper requires a control law capable of adapting this perceptually defined gradient vector field to the limited control authority of the physical robot with no loss of convergence yet retaining obstacle avoidance guarantees.

A. Beacon Landmarks and their Associated Camera Maps

We start by describing a visual sensor designed to observe the position of three known artificial beacons that comprise a landmark. We use the term "beacon" to denote any perceptually reliable marker that offers fixed bearing information. Our beacons are "artificial" — brightly colored objects that easily stand out against natural outdoor settings, depicted in figure 1

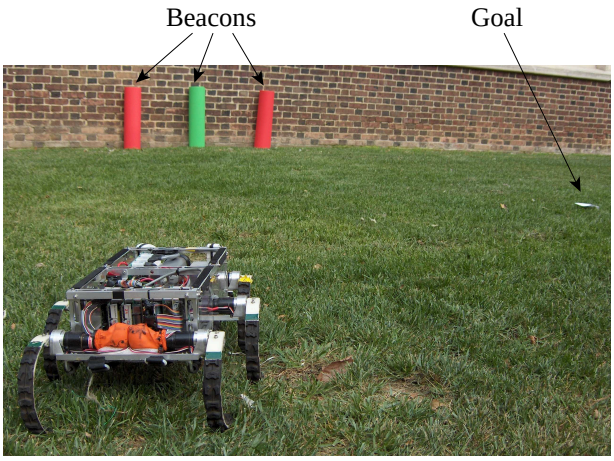

Fig. 1. The visual servoing problem: the robot RHex aims to reach the goal navigating using the colored beacons for visual cues.

— because we seek to avoid the well known problems of early vision that lie outside the intended scope of present work. We use the term "landmark" to denote the composition of three beacons into a source of sensory information sufficient to extract and regulate full relative pose on the plane. This point of view represents an adaptation and slight generalization of the fixed camera, moving beacon visual servoing algorithms introduced by Cowan *et al* [10]. In contrast, we address the "inside out" version of that problem arising from the task of registering a mobile robot vehicle[3] relative to some landmark in the visual field. The resulting camera map incorporates (a transformed copy of) the full relative pose and its gradient will be used to generate a servo controller that forces convergence to (some arbitrarily small specified neighborhood of) any desired visible pose along "safe" transients guaranteed to maintain the view along the way.

For purposes of this paper, it is sufficient to identify a beacon with the location of its centroid projected onto the plane. Given three such centroids, without any loss of generality, we define their composed landmark parameter space $\mathcal{B} \subset (\mathbb{R}^+)^2 \times \mathbb{S}^1$ by fixing the world frame so that the second beacon is at the origin and the remaining beacons lie along lines going through the origin that define congruent angles: $\mathcal{B} := \{(\rho_1, \rho_2, \alpha) \in (\mathbb{R}^+)^2 \times \mathbb{S}^1 \mid \rho_1 > 0, \rho_2 > 0, 0 \leq \alpha < \pi\}$ (see figure 2(a)). The coordinates of each beacon b_i in the world frame are:

$$\begin{bmatrix} b_1 & b_2 & b_3 \end{bmatrix} = \begin{bmatrix} \rho_1 R_\alpha \hat{e}_2 & \mathbf{0} & \rho_2 R_\alpha^T \hat{e}_2 \end{bmatrix}, \qquad (1)$$

where $R_\alpha = [\cos(\alpha) \ -\sin(\alpha); \sin(\alpha) \ \cos(\alpha)]$ is the standard 2×2 rotation matrix and $\hat{e}_2$ is the canonical base vector $[0\ 1]^T$. We define the *camera map* to be a transformation that relates the pose (position and orientation) of the robot in the world frame ($\mathsf{SE}(2)$) to the pinhole projection of the beacons in the camera's image plane.

For convenience, we treat the camera image plane as (a subset of) the unit sphere, $\mathbb{S}^2$, and drop the azimuthal component, thereby projecting all pinhole camera readings onto

[3] We assume that the camera is fixed to the robot's frame.

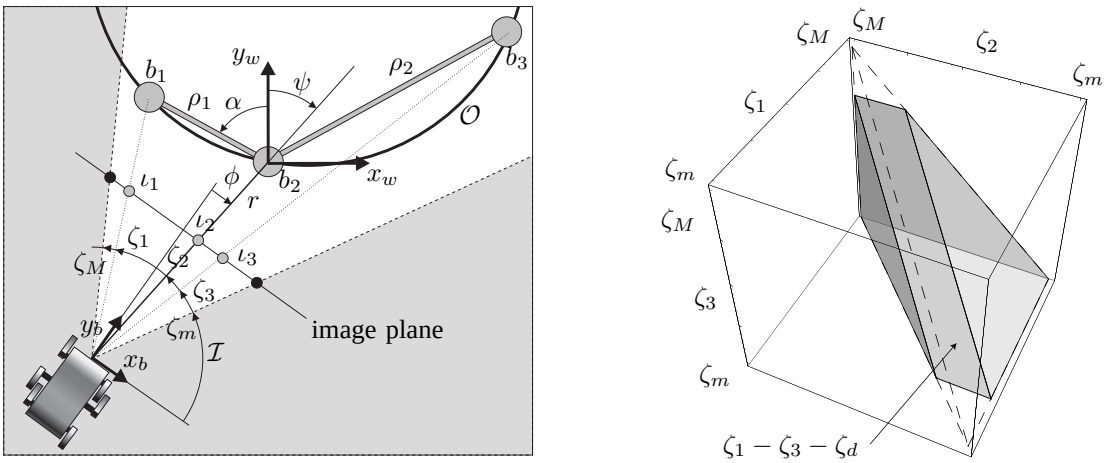

(a) (b)

Fig. 2. Simply connected configuration space introduced by Cowan *et al.* **a)** The beacons are represented by the gray circles named (b_1, b_2, b_3). **b)** Configuration space plotted in the Image projection space.

the great circle, $\mathbb{S}^1 \subset \mathbb{S}^2$, corresponding to bearing in the horizontal plane. In this manner, a beacon's pinhole image is parameterized by the angle of the ray that connects it to the camera center when projected onto the horizontal plane. We denote by $\mathcal{I}$ this image projection space — the triple of angles of each of the beacons in a landmark. Note that, although a physical camera has a flat image plane, we prefer to work with a ray's angle computed by the transformation $\zeta_i = \arctan(\iota_i) + \pi/2$, where ζ_i is the ith angle and ι_i is the coordinate measured by the camera in meters (after pre-processing using a lens calibration model), as illustrated in figure 2(a).

Because subsequent computations involving robot pose associated with the camera map are most easily expressed in polar coordinates, we find it expedient to introduce a new space[4], $\mathcal{C} \subset \mathbb{T}^2 \times \mathbb{R}^+$, diffeomorphic to the robot configuration space with coordinates $w = (\phi, \psi, r)$ (see figure 2(a)), where $\mathbb{T}^2$ is the 2-dimensional torus. To reconstruct the pose of the robot in the world frame, with coordinates (x_w, y_w, θ_w), a composition of changes of coordinates is implemented. We denote the change of coordinates from the intermediate space to the image projection space by *intermediate camera map* $c^{ci} : \mathcal{C} \to \mathcal{I}$,

$$c^{ci}(w) := \begin{bmatrix} \arctan(\varrho_1(w)) \\ \arctan(\varrho_2(w)) \\ \arctan(\varrho_3(w)) \end{bmatrix}, \tag{2}$$

where the terms $\varrho_i : \mathcal{C} \to \mathbb{R}^2$, defined by

$$\varrho_i(w) := R_\phi R_\psi b_i + r R_\phi \hat{e}_2, \tag{3}$$

are vectors that go through beacons b_i for a given configuration w and the function $\arctan$ is assumed to take into account which quadrant its argument is in. It can be shown that c^{ci} defines a diffeomorphism in $\mathcal{C}$ almost everywhere[5]. (for proof see [33]). The determinant of the Jacobian of the intermediate camera map ($|D_w c^{ci}| = \rho_1 \rho_2 \Theta \|\varrho_1\|^{-2} \|\varrho_3\|^{-2}$) gives a measure of the quality of the pose reconstruction. Here, the function $\Theta : \mathcal{B} \times \mathcal{C} \to \mathbb{R}$ defined by $\Theta(w) := \rho_1 \sin(\alpha - \psi) + \rho_2 \sin(\alpha + \psi) + r \sin(2\alpha)$ parameterizes the obstacle set $\mathcal{O}$ in which the intermediate camera map c^{ci} is not a valid change of coordinates. The set $\mathcal{O}$ is represented by a torus in $\mathcal{C}$ and only disconnects the robot's workspace for concave beacon configurations [33]. This exemplifies the dependence of the pose computation afforded by a given landmark upon the particular physical configuration of its constituent beacons. For convenience, in this paper, we maintain a linear beacon configuration since it proves to result in the largest robot workspace. The final camera map from world coordinates $\mathsf{SE}(2)$ to image projection $\mathcal{I}$ is:

$$c := c^{ci} \circ c^{bc} \circ c^{wb}, \tag{4}$$

where $c^{bc} : \mathsf{SE}(2) \to \mathcal{C}$ maps the body frame, with coordinates (x_b, y_b, θ_b), to the intermediate space $\mathcal{C}$ and $c^{wb} : \mathsf{SE}(2) \to \mathsf{SE}(2)$ maps the world frame to body frame. For their definition please see Appendix I.

The use of the intermediate space $\mathcal{C}$ provides a simple closed form expression for $(c^{ci})^{-1}$, the camera map inverse valid in $c^{ci}(\mathcal{C} - \mathcal{O})$. To compute $(c^{ci})^{-1}$, let the angles of the rays that connect the beacons to the camera center be $(\zeta_1, \zeta_2, \zeta_3) \in \mathcal{I}$ (i.e. $\zeta_i = \arctan(\iota_i) + \pi/2$) and let Y and Y' be:

$$Y = \begin{bmatrix} \cos(\zeta_1) & \cos(\zeta_2) & \cos(\zeta_3) \\ \sin(\zeta_1) & \sin(\zeta_2) & \sin(\zeta_3) \end{bmatrix} \tag{5}$$

$$Y' = \begin{bmatrix} \rho_1 \cos(\zeta_1 - \alpha) & 0 & \rho_2 \cos(\zeta_3 + \alpha) \\ \rho_1 \cos(\zeta_1 - \alpha) & 0 & \rho_2 \cos(\zeta_3 + \alpha) \end{bmatrix} \tag{6}$$

The robot's pose in $\mathcal{C}$ is computed by the following expressions, where $Y^\dagger := (YY^T)^{-1}Y$ is the pseudo-inverse of Y^T and $Y_\perp$ is the orthogonal complement to the span of $Y^\dagger$, computed by the cross product of the lines of $Y^\dagger$. The inverse intermediate camera map, with detailed computation

[4]The introduction of the intermediate space $\mathcal{C}$ distinguishes the present construction [33] from the one implemented in [10].

[5]We use the term "almost everywhere" in its standard sense as denoting a condition that holds true on all elements of a set except, possibly, for a zero measure subset.

in Appendix II, is:

$$\begin{aligned} \phi &= \zeta_2 + \frac{\pi}{2} \\ \psi &= \arctan(\delta R_\phi^T J Y' Y_\perp) \\ r &= \frac{\|Y^\dagger Y'^T J Y' Y_\perp\|}{\|Y' Y_\perp\|} \end{aligned} \tag{7}$$

where $\delta = \pm 1$ is chosen so that $-\pi/2 < \psi < \pi/2$, J is the 2×2 skew symmetric matrix $J := R_{\pi/2}$ and the function $\arctan$ takes into account the quadrant of its argument. The remainder maps c^{bc} and c^{wb} have simple inverse functions, expressions for which are explicitly provided in Appendix I. Using the previous closed form expression for the inverse camera map allows an efficient implementation of the pose computation algorithm on the robot.

B. Navigation Functions over the Visibility Set of a Landmark

The camera map previously defined introduces, in a physical implementation, "obstacles" to the robot's camera. The camera has a finite field of view and beacons' self-occlusions disrupt the image processing algorithm detailed in Section IV. Therefore a Navigation Function is introduced to deal with such obstacles. Let $\mathcal{Q}$ be a smooth, piecewise analytic, compact, connected manifold, with boundary $\partial\mathcal{Q}$ and let $q, q^* \in \mathcal{Q}$.

Definition 1 (Koditschek [34]): A Navigation Function is a C^2 Morse function, $\varphi : \mathcal{Q} \to [0, 1]$, having the additional properties that $\varphi^{-1}[0] = q^*$ is the unique minimum and the boundary with the forbidden configurations is set uniformly high, $\varphi^{-1}[1] = \partial\mathcal{Q}$.

Such functions are guaranteed to exist [12], and we assume that one is available in the present setting. Consider the following potential function $\bar{\bar{\varphi}} : \mathcal{I} \to \mathbb{R}^+$,

$$\bar{\bar{\varphi}} := \frac{\left((\zeta_1 - \zeta_1^*)^2 + (\zeta_2 - \zeta_2^*)^2 + (\zeta_3 - \zeta_3^*)^2\right)^k}{(\zeta_M - \zeta_1)(\zeta_1 - \zeta_2)(\zeta_2 - \zeta_3)(\zeta_3 - \zeta_m)(\zeta_1 - \zeta_3 - \zeta_d)},$$

For the previous potential function we consider the following:

- The vector $(\zeta_1^*, \zeta_2^*, \zeta_3^*)$ defines the goal in the image projection space $\mathcal{I}$, normally measured by taking a "snapshot" of the beacons at the desired position.
- k is a positive constant scalar shaping. In both simulations and experiments we take $k = 1$. For more information on the shaping parameter see [35].
- ζ_m and ζ_M are the field of view obstacles. These are computed based on the aperture of the camera's lenses.
- The denominator encodes the obstacles by "exploding" $\bar{\bar{\varphi}}$ when the 1st beacon reaches the left FOV $(\zeta_M - \zeta_1)$; the 1st and 2nd beacon intercept $(\zeta_1 - \zeta_2)$ and so forth. Notice that since the beacon angles are ordered in the image projection space then the beacons 1 and 3 cannot intercept unless 1 and 2 or 2 and 3 intercept first, allowing this way to simplify the denominator of the navigation function.
- The term $(\zeta_1 - \zeta_3 - \zeta_d)$ is introduced to limit the distance away from the set of beacons, where ζ_d is a positive scalar. Notice that the difference of the angles $\zeta_1 - \zeta_3$ will become smaller as the robot increases its distance from the beacons. The following formula gives a rough idea of how to approximately compute the parameter ζ_d given the distance between beacons 1 and 3, denoted by d_b, and the robot's maximum distance away from the beacons, denoted by d_{max}, both with units in meters:

$$\zeta_d = 2 \arcsin\left(\frac{d_b}{2 d_{max}}\right)$$

By construction $\bar{\bar{\varphi}}$ explodes at the obstacles and is zero at the goal. The resulting navigation function $\bar{\varphi} : \mathcal{I} \to [0, 1]$ is the squashed version of $\bar{\bar{\varphi}}$, with constant shaping scalar $\kappa > 0$:

$$\bar{\varphi} := \frac{\bar{\bar{\varphi}}}{\kappa + \bar{\bar{\varphi}}} \tag{8}$$

In the world frame the navigation function φ is the composition

$$\varphi(q) := \bar{\varphi} \circ c(q) \tag{9}$$

and the gradient is the pullback: $\nabla\varphi(q) = Dc^T(q) \nabla\bar{\varphi} \circ c(q)$. Let $\mathcal{Q}_I$ be the convex hull generated by the planes defined by the terms in the denominator of $\bar{\bar{\varphi}}$, i.e. $\zeta_M - \zeta_1 = 0$, $\zeta_1 - \zeta_2 = 0$, etc, illustrated in figure 2(b). The robot's configuration space is defined by:

$$\mathcal{Q} := c^{-1}(\mathcal{Q}_I) \tag{10}$$

C. The "Unicycle" Robot Motion Model

The physical implementation of the algorithms presented in this paper are carried out on the hexapod robot RHex, whose horizontal plane behavior is known from empirical experience to be roughly modeled as a quasi-static unicycle. Therefore we recall the equations of motion of the unicycle, extensively studied in the literature [36], with $q = (x, y, \theta)$:

$$\begin{aligned} \dot{x} &= -\sin(\theta) u_1 \\ \dot{y} &= \cos(\theta) u_1 \\ \dot{\theta} &= u_2 \end{aligned} \tag{11}$$

The nonholonomic constraint is $A(q)\dot{q} = 0$, where

$$A(q) = \begin{bmatrix} \cos(\theta) & \sin(\theta) & 0 \end{bmatrix} \tag{12}$$

Notice that the nonholonomic constraints of the unicycle preclude the direct use of the navigation function gradient vector field. We proceed by solving this problem in general for systems defined in $\mathbb{R}^3$.

III. Hybrid controller to solve the visual servoing problem

Here we present a set of verifiable conditions that guarantee stabilization for the successive application of a two step controller: the first moves on level sets of the gradient function, escaping the center manifold and if possible reaching the goal's stable manifold; the second uses the gradient control law to reach the goal.

Let $q = (x_1, x_2, x_3) \in \mathcal{Q} \subset \mathbb{R}^3$ and consider the class of smooth and piecewise analytic, three degree of freedom, drift-free control systems

$$\dot{q} = B(q)u, \quad u \in \mathbb{R}^2, \tag{13}$$

where $B \in \mathbb{R}^{3\times 2}$ and $\mathcal{Q}$ is a smooth and piecewise analytic, compact[6], connected three dimensional manifold with a boundary, $\partial\mathcal{Q}$ (that separates the acceptable from the forbidden configurations of $\mathbb{R}^3$), possessing a distinguished interior *goal point*, $q^* \in \mathcal{Q}$. In this section we will impose very general assumptions on B and construct a hybrid controller that guarantees local convergence to an arbitrarily small neighborhood of the goal state while avoiding any forbidden configurations along the way.[7]

We find it convenient to rewrite (13) using the *nonholonomic projection matrix* [37], H into the image of B:

$$H(q) = B(q)B(q)^\dagger = B(q)\left(B(q)^T B(q)\right)^{-1} B(q)^T \tag{14}$$

$$\dot{q} = H(q)v, \quad q \in \mathcal{Q} \subset \mathbb{R}^3; \quad v \in \mathbb{R}^3 \tag{15}$$

Throughout this paper it is assumed that B has rank two at each point.

A. Two controllers and their associated closed loop dynamics

It is useful to compare the unconstrained system $\dot{q} = v$ with the constrained version (15). Let φ be a navigation function defined in $\mathcal{Q}$. For the input $v = -\nabla\varphi$ the unconstrained system is globally asymptotically stable at the origin. Using φ as a control Lyapunov function yields $\dot{\varphi} = -\|\nabla\varphi\|^2$. Given this result, a naive approach to attempt stabilizing system (15) is to use the same input $v = -\nabla\varphi$.

Define the vector field $f_1 : \mathcal{Q} \to T\mathcal{Q}$ such that $f_1(q) := -H(q)\nabla\varphi(q)$ and the system

$$\dot{q} = f_1(q) = -H(q)\nabla\varphi(q) \tag{16}$$

Since H has a 1-dimensional kernel and $D^2\varphi$ is full rank at q^* it follows that (16) has a 1 dimensional center manifold

$$\mathcal{W}^c := \{q \in \mathcal{Q} : H(q)\nabla\varphi(q) = 0\}, \tag{17}$$

as corroborated by explicitly computing[8] the Jacobian of f_1 at q^*:

$$Df_1|_{q^*} = -DH \underbrace{\nabla\varphi|_{q^*}}_{=0} - HD^2\varphi = -\left. HD^2\varphi\right|_{q^*} \tag{18}$$

Using φ as a Lyapunov function, and noting that H is idempotent and symmetric, La Salle's invariance theorem states that system (16) has its limit set in $\mathcal{W}^c$:

$$\begin{aligned}\dot{\varphi} &= -\nabla\varphi^T H \nabla\varphi \\ &= -\|H\nabla\varphi\|^2 \begin{cases} = 0 & \text{if} \quad q \in \mathcal{W}^c \\ < 0 & \text{if} \quad q \notin \mathcal{W}^c \end{cases}\end{aligned} \tag{19}$$

[6]We consider the configuration space $\mathcal{Q}$ to be a compact set since this requirement is built into the definition of a navigation function. The changes of coordinates for the camera maps are mostly defined in $\mathsf{SE}(2)$ because they are valid there. In general, as in the present application, due to the limitations of the vision sensors, the workspace is always bounded, hence its closure is compact.

[7]In the next section, we will introduce more specialized assumptions that extend the basin of attraction to include almost every initial configuration in $\mathcal{Q}$.

[8]Note the abuse of notation in equation (18): DH is actually a tensor.

Figure 3 illustrates the topology associated with (16): the projection H imposes a co-dimension 1 foliation complementary to the center manifold. The *stable manifold*, $\mathcal{W}^s$, is the leaf containing the goal, q^*. The input

$$u_1 := -B(q)^\dagger \nabla\varphi(q) \tag{20}$$

alone cannot stabilize system (16) at the origin, since no smooth time invariant feedback controller has a closed loop system with an asymptotically stable equilibrium point [14]. Nevertheless, for any initial condition outside $\mathcal{W}^c$ an infinitesimal motion in the direction of f_1 reduces the energy φ. If there can be found a second controller that "escapes" $\mathcal{W}^c$ without increasing φ then it is reasonable to imagine that iterating the successive application of these two controllers might well lead eventually to the goal. We now pursue this idea by introducing the following controller,

$$u_2 := B(q)^\dagger \left[A(q) \times \nabla\varphi(q)\right], \tag{21}$$

leading to the closed loop vector field[9]

$$\begin{aligned}\dot{q} &= H(q)f_2(q) = f_2(q) \\ f_2(q) &:= A(q) \times \nabla\varphi(q)\end{aligned} \tag{22}$$

where $A(q)$ can be computed by the normalized cross product of the columns of $B := [B_1\ B_2]$:

$$A(q) := \frac{B_1 \times B_2}{\|B_1 \times B_2\|} \tag{23}$$

Note that the nonholonomic constraint expressed in (13) can be represented by the implicit equation $A^T(q)\dot{q} = 0$. Since the (Lie) derivative of φ in the direction of f_2 is

$$L_{f_2}\varphi = \nabla\varphi(q)^T(A(q) \times \nabla\varphi(q)) = 0, \tag{24}$$

it follows that f_2 is φ-invariant — i.e. the energy, φ, is constant along its motion. Moreover $Hf_2 = (I - AA^T)(A \times \nabla\varphi) = A \times \nabla\varphi = f_2$, verifying that f_2 indeed satisfies the constraint (13).

B. Assumptions, a Strategy, and Preliminary Analysis

Having introduced two vector fields — one which is energy decreasing; the other energy conserving — we now sketch a strategy that brings initial conditions of system (13) to within an arbitrarily small neighborhood ϵ of the goal, by way of motivating the subsequent definitions and claims that arise in the formal proofs to follow. Let $\Phi_t^{f_1}$ and $\Phi_t^{f_2}$ denote the flows of f_1 and f_2 respectively. The point stabilization strategy is as follows:

1) If $q_0 \in \mathcal{W}^c$ then follow a direction in $\mathrm{im}(H)$ for a finite amount of time t_0 such that $\Phi_{t_0}^{fa}(q_0) \notin \mathcal{W}^c$ and $\varphi \circ \Phi_{t_0}^{fa}(q_0) < 1$ for all $t \in (0, t_0)$.

2) If $q_0 \notin \mathcal{W}^c$ and $\varphi(q_0) > \epsilon$
   2.1) Use a scaled version of f_2 for time τ_2 to escape a δ-neighborhood of $\mathcal{W}^c$, keeping the energy φ constant.

[9]Below we show that $\forall q : Hf_2 = f_2$

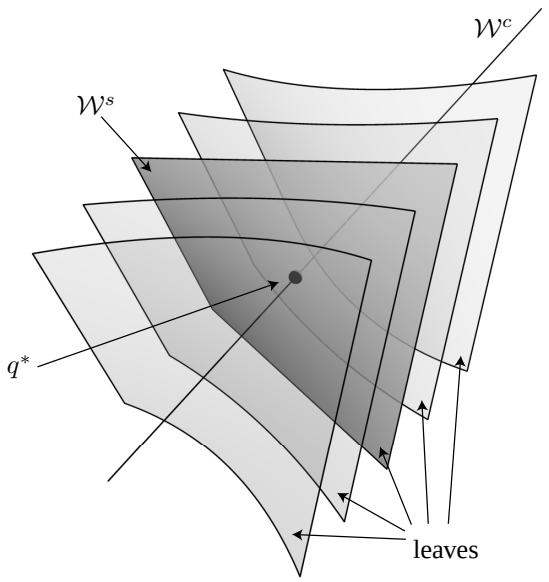

Fig. 3. Conceptual illustration of the flow associated with equation (16). Each leaf is an invariant manifold with all trajectories collapsing into $\mathcal{W}^c$.

2.2) Use controller f_1, for time τ_1, to decrease the energy φ, stopping at a γ-neighborhood of $\mathcal{W}^c$ such that $\Phi^{fa}_{\tau_1}(q) \notin \mathcal{W}^c$ and $\gamma < \delta$.

We now introduce a number of assumptions, definitions and their consequences that will allow us to formalize each of the previous steps. The reader less interested in the formal proof can skip to the end of Section III-C.

A1 $\mathcal{Q}$ is a smooth compact connected manifold with boundary.

A2 φ is a navigation function in $\mathcal{Q}$.

A3 H has rank two, uniformly throughout $\mathcal{Q}$.

Assumption A1 gives the proper setting for the existence of a navigation function in the configuration space. Assumption A3 assures the foliation sketched in figure 3.

Define the *local surround* of the goal, illustrated in figure 4, to be the closed "hollow sphere", $\mathcal{Q}_s := \varphi^{-1}[I_{\epsilon s}]$, with $I_{\epsilon s} := [\epsilon, \varphi_s]$ whose missing inner "core" is the arbitrarily small open neighborhood, $\mathcal{Q}_\epsilon := \varphi^{-1}[I_{0\epsilon}]$; $I_{0\epsilon} := [0, \epsilon)$, and whose outer "shell", $\mathcal{Q}_1 := \varphi^{-1}[I_{s1}]$, with $I_{s1} := (\varphi_s, 1]$, includes the remainder of the free configuration space. φ_s is defined to be the largest level such that all the smaller levels, $\varphi_0 \in (0, \varphi_s)$ are homeomorphic to the sphere, $\mathbb{S}^2$, and are all free of critical points, $\|\nabla\varphi\|^{-1}[0] \cap \varphi^{-1}[(0, \varphi_s)] = \emptyset$.

The restriction to φ-invariant topological spheres precludes limit sets of f_2 more complex than simple equilibria in the local surround. In the examples of Sections III-F and III-H, we provide more specialized conditions that allow us to guarantee that the algorithm brings almost every initial condition in the "outer" levels, $\mathcal{Q}_1$ into the local surround, $\mathcal{Q}_s$ and, thence, into the goal set $\mathcal{Q}_\epsilon$.

Lemma 1: Given the previous assumptions

$$f_1^{-1}[0] \cap \mathcal{Q}_s \equiv f_2^{-1}[0] \cap \mathcal{Q}_s \equiv \mathcal{W}^c \cap \mathcal{Q}_s. \tag{25}$$

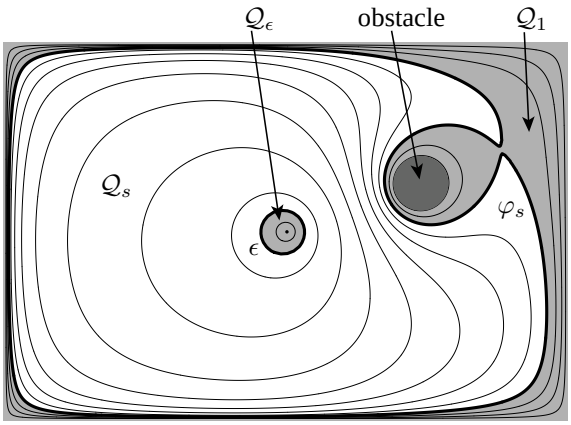

Fig. 4. Illustration of the local surround $\mathcal{Q}_s$ of the goal in white. The thin lines represent various levels of φ. This image is presented in the plane for readability purpose. However it should be interpreted as a section of $\mathcal{Q} \subset \mathbb{R}^3$

Proof: If $q \in f_2^{-1}[0]$ then $\nabla\varphi = \alpha A$, where α is a non-zero scalar, hence $\nabla\varphi \in \ker H$ and $q \in \mathcal{W}^c$ as defined by (17). ■

To formally express the "δ-neighborhood" of $\mathcal{W}^c$ described in the stabilization strategy we start by defining the function $\xi : \mathcal{Q} - \{q^*\} \to [0, 1]$:

$$\xi(q) := \frac{\|H(q)\nabla\varphi(q)\|^2}{\|\nabla\varphi(q)\|^2} \tag{26}$$

The quantity $\|H(q)\nabla\varphi(q)\|^2$ evaluates to zero only in $\mathcal{W}^c - \{q^*\}$. Therefore in a small neighborhood of $\mathcal{W}^c$ the level sets of $\|H(q)\nabla\varphi(q)\|^2$ define a "tube" around $\mathcal{W}^c$. The denominator of (26) normalizes ξ such that $0 \le \xi \le 1$. Moreover it produces a "pinching" of the tube at the goal q^*.

Lemma 2: For all $\varphi_0 \in I_{\epsilon s}$, $\varphi^{-1}[\varphi_0]$ intersects the unit level set of ξ, i.e., $\xi^{-1}[1] \cap \varphi^{-1}[\varphi_0] \neq \emptyset$.

Proof: Observe that $\xi(q) = 1$ is equivalent to the condition $\nabla\varphi^T Q \nabla\varphi = 0$ where $Q := I - H$. Now consider the family of vector fields

$$h_\alpha(q) := -[Q(q) + \alpha H(q)]\nabla\varphi(q), \tag{27}$$

$$\dot{q} = h_\alpha(q), \tag{28}$$

Note, for $\alpha > 0$ the goal point q^* is globally asymptotically stable over the domain $\mathcal{Q}_\epsilon \cup \mathcal{Q}_s$, since φ is a Lyapunov function for (28),

$$\begin{aligned}\dot{\varphi} &= -\nabla\varphi^T(Q + \alpha H)\nabla\varphi = \\ &= -\nabla\varphi^T(Q(1-\alpha) + \alpha I)\nabla\varphi = \\ &= -(1-\alpha)\nabla\varphi^T Q\nabla\varphi - \alpha\|\nabla\varphi\|^2 \le -\alpha\|\nabla\varphi\|^2\end{aligned}$$

and φ has no other critical points other than q^* in $\mathcal{Q}_\epsilon \cup \mathcal{Q}_s$.

Next, observe that $\xi^{-1}[1] = \mathcal{W}_h^0$ is a center manifold for h_0. Hence, according to Fenichel's Singular Perturbation Theorem (see Appendix III for a careful statement and citation) there persists a "slow stable manifold" of h_α, $\mathcal{W}_h^\alpha$, that is arbitrarily close to $\xi^{-1}[1]$ as the positive scalar α approaches 0. Configurations $q_0 \in \varphi^{-1}[\epsilon] \cap \mathcal{W}_h^\alpha$, that are arbitrarily close to q^* on this invariant set are associated with reverse

time trajectories $\Phi_{-t}^{h_\alpha}(q_0)$ that pass through every level set $\varphi^{-1}[\varphi_0]$, for $\varphi_0 \in I_{\epsilon s}$ since $\dot{\varphi} \circ \Phi_t^{h_\alpha}(q_0) < 0$ according to the previous paragraph. It follows that $\mathcal{W}_h^\alpha$ intersects every level set, $\varphi^{-1}[\varphi_0]$, for $\varphi_0 \in I_{\epsilon s}$ for $\alpha = 0$ as well. ■

Corollary 1: For all $\varphi_0 \in I_{\epsilon s}$ the level set $\varphi^{-1}[\varphi_0]$ intersects every level set of ξ, i.e., $\xi^{-1}[\alpha] \cap \varphi^{-1}[\varphi_0] \neq \emptyset$ for all $\alpha \in [0,1]$.

Proof: Choose $q_1 \in \xi^{-1}[1] \cap \varphi^{-1}[\varphi_0]$ as guaranteed to exist by Lemma 2. Choose $q_0 \in \xi^{-1}[0] \cap \varphi^{-1}[\varphi_0]$ as guaranteed to exist since $\xi^{-1}[0]$ coincides with $\mathcal{W}^c$, the center manifold of f_1, which intersects each level set $\varphi^{-1}[\varphi_0]$ twice. Since for all $\varphi_0 \in I_{\epsilon s}$ the set $\varphi^{-1}[\varphi_0]$ is simply connected then there can be found a continuous curve, $c : [0,1] \to \varphi^{-1}[\varphi_0]$ connecting q_0 and q_1. The function $\xi \circ c(\alpha)$ must vary continuously between 0 and 1 and the result follows as claimed. ■

Lemma 3: A sufficient condition for the Jacobian of $f_2(q)$ evaluated at $\mathcal{W}^c - \|\nabla\varphi\|^{-1}[0]$ to have at least one eigenvalue with non-zero real part is that the control Lie algebra on B spans $\mathbb{R}^3$.

Proof: Let $J(A)$ be the 3×3 skew symmetric matrix associated with A. We will show that the rank condition implies a nonvanishing trace by explicitly computing the eigenvalues of $Df_2|_{\mathcal{W}^c}$:

$$\begin{aligned} Df_2 &= J(A)D^2\varphi - J(\nabla\varphi)DA \\ Df_2|_{\mathcal{W}^c} &= J(A)[D^2\varphi - \|\nabla\varphi\|DA] \end{aligned}$$

Now consider the change of coordinates $R = [A, A_\perp]$, where R defines a rotation matrix and $A_\perp = [A_2 \ A_3]$ are orthogonal to A. Find the eigenvalues of Df_2:

$$\begin{aligned} &\det(Df_2 - \lambda I_3) = \det(R^T Df_2 R - \lambda I_3) \\ &= \det\left(\begin{bmatrix} 0 \\ A_\perp^T J(A) \end{bmatrix} [D^2\varphi - \|\nabla\varphi\|DA]R - \lambda I_3 \right) \end{aligned}$$

Using Cramer's rule we obtain:

$$= -\lambda \det\left(A_\perp^T J(A)[D^2\varphi - \|\nabla\varphi\|DA]A_\perp - \lambda I_2\right)$$

One zero eigenvalue can be immediately factored out from the previous expression leaving as the second factor the characteristic polynomial of a 2×2 matrix whose trace we compute as:

$$\begin{aligned} &\text{trace}\left(A_\perp^T J(A)[D^2\varphi - \|\nabla\varphi\|DA]A_\perp\right) \\ &= \text{trace}\left(A_\perp^T J(A) D^2\varphi A_\perp\right) + \\ &\quad -\|\nabla\varphi\|\text{trace}\left(A_\perp^T J(A) DAA_\perp\right) \end{aligned} \tag{29}$$

Since $D^2\varphi$ is symmetric the first term in the sum just presented can be shown to vanish by noting:

$$\begin{aligned} &\text{trace}\left(A_\perp^T J(A) D^2\varphi A_\perp\right) = \\ &= \text{trace}\left(\begin{bmatrix} A_2^T \\ A_3^T \end{bmatrix} J(A) D^2\varphi \begin{bmatrix} A_2 & A_3 \end{bmatrix} \right) \\ &= \text{trace}\left(\begin{bmatrix} A_3^T \\ -A_2^T \end{bmatrix} D^2\varphi \begin{bmatrix} A_2 & A_3 \end{bmatrix} \right) \\ &= A_3^T D^2\varphi A_2 - A_2^T D^2\varphi A_3 = 0 \end{aligned}$$

Equation (29) becomes:

$$\begin{aligned} &= -\|\nabla\varphi\|\text{trace}\left(A_\perp^T J(A) DAA_\perp\right) \\ &= -\|\nabla\varphi\| A_3^T (DA - DA^T) A_2 \end{aligned} \tag{30}$$

Since $A^T A_2 \equiv 0$ and $A^T A_3 \equiv 0$ we obtain the relations, using the Lie derivative:

$$\begin{aligned} L_{A_3}(A^T A_2) &= \left(A_2^T DA + A^T DA_2\right) A_3 = 0 \\ L_{A_2}(A^T A_3) &= \left(A_3^T DA + A^T DA_3\right) A_2 = 0 \end{aligned}$$

Replacing the previous relations into (30) we obtain:

$$\begin{aligned} &-\|\nabla\varphi\| A_3^T (DA - DA^T) A_2 \\ &= -\|\nabla\varphi\| \left(A^T DA_2 A_3 - A^T DA_3 A_2\right) \\ &= -\|\nabla\varphi\| A^T [A_2, A_3] \end{aligned} \tag{31}$$

Since the span of $\{A_2, A_3\}$ is equal to the span of $\{B_1, B_2\}$ then there exist continuous functions $\alpha_i(q), \beta_i(q)$ such that $A_i = \alpha_i B_1 + \beta_i B_2$, and (31) becomes

$$\begin{aligned} &= -\|\nabla\varphi\| A^T \left((\alpha_2\beta_3 - \alpha_3\beta_2)[B_1, B_2] + M_1 B_1 + M_2 B_2\right) \\ &= \gamma(q) A^T [B_1, B_2], \end{aligned}$$

where M_1, M_2 are matrix functions with left kernel A that contain derivatives of α_i, β_i and $\gamma(q) \neq 0, \ \forall q \notin \|\nabla\varphi\|^{-1}[0]$ is a continuous function. If the matrix $|B_1 \ B_2 \ [B_1, B_2]|$ is full rank then $A^T[B_1, B_2] \neq 0$. ■

Lemma 4: The Jacobian of $f_2(q)$ evaluated at $\mathcal{W}^c \cap \mathcal{Q}_s$ has two non-zero real part eigenvalues with the same sign.

Proof: Let $\mathcal{L}_\alpha = \varphi^{-1}[\alpha], \ \alpha < \varphi_s$. The function $f_2|_{\mathcal{L}_\alpha}$ is a flow on a topological sphere. By lemma 1 and corollary 1 it only has two critical points with index $+1$ (Poincaré-Hopf [38]). Therefore $Df_2|_{\mathcal{W}^c \cap \mathcal{Q}_s}$ has two non-zero real part eigenvalues with the same sign. ■

Now consider the implicit equation,

$$\xi(q) = \xi^* \Leftrightarrow \|H(q)\nabla\varphi(q)\|^2 = \xi^* \|\nabla\varphi(q)\|^2 \tag{32}$$

At the goal any ξ^* satisfies (32). Although ξ is not defined at q^* all of its level sets intersect at q^*. Finally, define the parameterized cone $\mathcal{C}_\gamma$ around $\mathcal{W}^c$, and its complement $\mathcal{C}_\gamma^c := \mathcal{Q} - \mathcal{C}_\gamma - \{q^*\}$, by:

$$\mathcal{C}_\gamma = \{q \in \mathcal{Q} - \{q^*\} : \xi(q) \leq \gamma\} \tag{33}$$

We follow by imposing conditions on H and A such that the vector field f_2 can afford the needed "escape" from $\mathcal{W}^c$.

Lemma 5: Suppose system (13) satisfies assumptions A1-A3 and, hence, the previous lemmas. Then, there exists a function $\sigma : \mathcal{Q} \to \mathbb{R}$ that renders the system

$$\dot{q} = \sigma(q) A(q) \times \nabla\varphi(q) = \bar{f}_2(q) \tag{34}$$

unstable at $\mathcal{W}^c \cap \mathcal{Q}_s$.

Proof: Let $\Xi : \mathcal{Q} \to \mathbb{C}; \ \Xi(q) \mapsto \max(\text{Re}(\{\lambda_1, \lambda_2, \lambda_3\}))$ return the eigenvalue with largest real part of the Jacobian of f_2 evaluated at the closest point to q that lives in $\mathcal{W}^c$. Consider the function $\sigma : \mathcal{Q}_s \to \mathbb{R}$ such that

$$\sigma(q) = \begin{cases} 1 & \text{if} \quad \text{Re}(\Xi(q)) > 0 \\ -1 & \text{if} \quad \text{Re}(\Xi(q)) \leq 0 \end{cases}$$

Partition $\mathcal{Q}_s$ into its two pieces, $\mathcal{Q}^+ = \{q \in \mathcal{Q}_s : \sigma(q) = 1\}$ and $\mathcal{Q}^- = \{q \in \mathcal{Q}_s : \sigma(q) = -1\}$ where $\mathcal{Q}^+ \cup \mathcal{Q}^- = \mathcal{Q}_s$ and $\mathcal{Q}^+ \cap \mathcal{Q}^- = \emptyset$.

In $\mathcal{W}^c \cap \mathcal{Q}^+$ two eigenvalues of $D\bar{f}_2$ have positive real part, rendering (34) unstable. In $\mathcal{W}^c \cap \mathcal{Q}^-$ we get that $D\bar{f}_2 = -Df_2$. Therefore the two nonzero real part eigenvalues of $D\bar{f}_2$ have a positive sign, also rendering (34) unstable. ■

Corollary 2: Under the conditions of the previous lemma, there can be found a $\tau \in (0, \infty)$ such that for all $q_0 \in \xi^{-1}[\delta/2]$ we have $\xi \circ \Phi_\tau^{\bar{f}_2}(q_0) \geq \delta$.

Proof: Since $\mathcal{W}^c \cap \mathcal{Q}_s$ is unstable, for every level $\mathcal{L}_\alpha$ with $\alpha < \varphi_s$ and $q_\alpha \in \mathcal{L}_\alpha \cap \mathcal{W}^c$ there exists an $\kappa^+(\alpha) > 0$ and a neighborhood $\mathrm{B}_{\kappa^+}(q_\alpha) := \{q \in \mathcal{Q}_s | \|q - q_\alpha\| \leq \kappa^+\}$ such that every trajectory of $\bar{f}_2$ with initial condition inside $\mathrm{B}_{\kappa^+}(q_\alpha) - \mathcal{W}^c$ will eventually leave $\mathrm{B}_{\kappa^+}(q_\alpha)$. Let δ be the largest scalar such that $\mathcal{C}_\delta \subset \mathcal{N}^+ := \bigcup_\alpha \mathrm{B}_{\kappa^+}(q_\alpha)$. Let $\kappa^- > 0$ be the largest scalar such that $\mathcal{N}^- := \bigcup_\alpha \mathrm{B}_{\kappa^-}(q_\alpha) \subset \mathcal{C}_\gamma$, with $2\gamma = \delta$. The set $\mathcal{N} := \mathcal{N}^+ - \mathrm{int}\,(\mathcal{N}^-)$ is compact. Therefore, since $\mathcal{N} \cap \mathcal{W}^c = \emptyset$, trajectories of f_1 and $\bar{f}_2$ traverse $\mathcal{N}$ in finite time. Let $\tau_0(q_0) := \min\{t > 0 \mid \xi \circ \Phi_t^{\bar{f}_2}(q_0) = \delta\}$. Then define $\tau := \max\{\tau_0(q_0) | q_0 \in \mathcal{N}\}$. ■

Figure 5 illustrates the steps used in the previous proof. Trajectories starting inside $\mathcal{N} - \mathcal{C}_\gamma^c$ will traverse $\partial\mathcal{C}_\gamma$ and $\partial\mathcal{C}_\delta$ in finite time.

C. A Hybrid Controller and Proof of its Local Convergence

Given the previous results define the time variables τ_1, τ_2 and the scalars $\gamma < \delta$ such that:

$$\tau_1(q, \gamma) := \begin{cases} \min\left\{t > 0 \mid \xi \circ \Phi_t^{f_1}(q) = \gamma\right\} & \text{if } q \in \mathcal{C}_\gamma^c \\ 0 \text{ otherwise} \end{cases}$$

$$\tau_2(q, \delta) := \begin{cases} \min\left\{t > 0 \mid \xi \circ \Phi_t^{\bar{f}_2}(q) = \delta\right\} & \text{if } q \in \mathcal{C}_\delta - \mathcal{W}^c \\ 0 \text{ otherwise} \end{cases}$$

I.e., τ_1 is the time to reach the γ neighborhood of $\mathcal{W}^c$ using vector field f_1 and τ_2 is the time to reach the boundary of $\mathcal{C}_\delta$ using vector field $\bar{f}_2$, escaping this way the γ neighborhood of $\mathcal{W}^c$.This results in the following maps:

$$\Phi_{\tau_1}^{f_1} \quad : \quad \overline{\mathcal{C}_\gamma^c} \to \partial\mathcal{C}_\gamma \tag{35}$$

$$\Phi_{\tau_2}^{\bar{f}_2} \quad : \quad \mathcal{Q}_s - \mathcal{W}^c \to \overline{\mathcal{C}_\delta^c} \subset \overline{\mathcal{C}_\gamma^c}, \tag{36}$$

where $\overline{\mathcal{C}}$ is the closure of $\mathcal{C}$. With $\delta = 2\gamma$ define the map $P : \mathcal{Q}_s - \mathcal{W}^c \to \partial\mathcal{C}_\gamma$

$$P(q) = \Phi_{\tau_1(\cdot,\gamma)}^{f_1} \circ \Phi_{\tau_2(q,2\gamma)}^{\bar{f}_2}(q) \tag{37}$$

and consider the recursive equation:

$$q_{k+1} = P(q_k). \tag{38}$$

The set $\partial\mathcal{C}_\gamma$ can be interpreted as a Poincaré section for the discrete system (38). We are now ready to present the final result:

Theorem 3: There exists an iteration number, $N : \mathcal{Q}_s \to \mathbb{N}$ such that the iterated hybrid dynamics, P^N brings $\mathcal{Q}_s$ to $\mathcal{Q}_\epsilon$.

Proof: Define

$$N := \min\left\{n \in \mathbb{N} | 0 \leq N \leq N_\epsilon | \varphi \circ P^n(q_0) \leq \epsilon\right\},$$

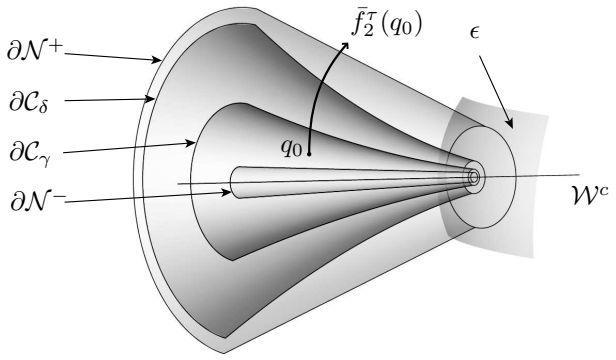

Fig. 5. Illustration of the construction used in the proof of corollary 2.

and $\Delta\varphi(q) := \varphi \circ P(q) - \varphi(q)$. Since $\mathcal{Q}_s$ is a compact set it follows that $|\Delta\varphi|$ achieves its minimum value, Δ_ϵ, on that set, hence at most $N_\epsilon := \text{ceiling}(\varphi_s - \epsilon)/\Delta_\epsilon$ iterations are required before reaching $\mathcal{Q}_\epsilon$. ■

Note that all initial conditions in the pre-image of the "local surround", $\mathcal{R} := \bigcup_{t>0} \Phi_{-t}^{f_1}(\mathcal{Q}_s - \mathcal{W}^c)$ are easily included in the basin of the goal, $\mathcal{Q}_s$, by an initial application of the controller u_1. While it is difficult to make any general formal statements about the size of $\mathcal{R}$, we show in the next section that for all the examples we have tried, the "missing" initial conditions, $\mathcal{Q} - \mathcal{R} = \mathcal{Z}$, comprise a set of empty interior (in all but one case $\mathcal{Z}$ is actually empty) because all of $\mathcal{W}^c$, excepting at most a set of measure zero, is included in $\mathcal{Q}_s$. In configuration spaces with more complicated topology, there is no reason to believe that this pleasant situation would prevail. To summarize, we rewrite the strategy presented in Section III-B using now the explicit input controls:

1) $\forall q_0 \in \mathcal{W}^c$ use the input
$$u_3 := \begin{bmatrix} \alpha_1 & \alpha_2 \end{bmatrix}^T, \tag{39}$$
for a small amount of time t_3, where α_1, α_2 are scalar constants not both simultaneously zero, such that $\varphi \circ \Phi_{t_3}^{f_3}(q_0) < 1$ and $\Phi_{t_3}^{f_3}(q_0) \notin \mathcal{W}^c$, with $f_3(q) := B(q)u_3$.
2) $\forall q_0 \in \mathcal{Q}_s - \mathcal{W}^c$, follow successive applications of (38), i.e. use the inputs to equation (13):
$$u_1(q) := -B^\dagger(q)\nabla\varphi(q) \tag{40}$$
$$u_2(q) := \sigma(q)B^\dagger(q)J(A(q))\nabla\varphi(q) \tag{41}$$
3) $\forall q_0 \in \mathcal{R} - \mathcal{Q}_s$, use the input u_1 for time t until $\Phi_t^{f_1}(q_0) \in \mathcal{Q}_s$.

Having discussed the volume of convergence, the next most crucial question bearing on the practicality of this scheme, speed of convergence, will also be addressed on a case by case basis in Section III-H using two additional formal ideas that we now present.

D. Limit cycles in the level sets of φ

In many practical applications switching between controllers f_1 and f_2 using a small δ-neighborhood is far too conservative. It may be possible to escape $\mathcal{W}^c$ by more than just the small collar $\xi^{-1}[\delta]$. In Section III-H we show an example where

the trajectories of f_2 flow from $\mathcal{W}^c \cap \varphi^{-1}[\varphi_0]$ with positive real part eigenvalues, where $\varphi_0 < \varphi_s$ is some energy, to $\mathcal{W}^c \cap \varphi^{-1}[\varphi_0]$ with negative real part eigenvalues, crossing in between the stable manifold at the goal $\mathcal{W}^s$. If we could recognize the passage into $\mathcal{W}^s$ and switch off controller u_2 (i.e. turn $\mathcal{W}^s$ into an attractor of a suitable modified form of f_2) then a final application of controller u_1 is guaranteed to achieve the goal state, q^*. The hope of reworking the form of u_2 so that the resulting closed loop vector field, f_2, has its forward limit set solely in $\mathcal{W}^s$ thus raises the question of when there exists limit cycles in the level sets of φ for the flow of f_2. More importantly, we seek a condition that guarantees that every trajectory of f_2 starting in a small neighborhood of $\mathcal{W}^c$ can intersect $\mathcal{W}^s$ either by forward or inverse time integration of system (22). Note that f_2 generates a planar flow, making the Bendixson's criteria a natural candidate for such condition. Several authors [39]–[42] have developed extensions to Bendixson's criteria for higher dimensional spaces, obtaining in general conditions that preclude invariant sub-manifolds on some set. For systems with first integrals, such as some classes of systems that result from nonholonomic constraints, the conditions simplify to a divergence style test. Fečkan's theorem (see Appendix IV and [39]) states that in open subsets where $\mathrm{div} f_2 \neq 0$ there can exist no invariant submanifolds of any level precluding cyclic orbits. Note that the previous result does not preclude quasi-periodic orbits. In Section III-G we give an example that, by having $\varphi_s < 1$, results in quasi-periodic orbits on a torus. Using Cauchy-Riemann the divergence of the vector field f_2 results in:

$$\begin{aligned} \mathrm{div}(f_2) &= \mathrm{div}\left(A(q) \times \nabla\varphi(q)\right) \\ &= \left(\nabla \times A(q)\right)^T \nabla\varphi(q) \\ &= A_R(q)^T \nabla\varphi(q) \end{aligned} \tag{42}$$

In the examples described here, the set $\mathcal{D} := \left\{q \in \mathcal{Q} : A_R(q)^T \nabla\varphi(q) = 0\right\}$ is a 2-manifold that contains the goal. If $\mathcal{D} \cap \mathcal{W}^c = \{q^*\}$ and $\mathcal{D}$ is not itself invariant for f_2 then we are guaranteed that there exist no limit cycles on the level sets of φ.

E. Computational heuristic substitutes for σ

The σ function introduced in lemma 5 modifies the flow of f_2 rendering the center manifold unstable. Having that property is sufficient for stabilization, but more can be accomplished. By careful craft of σ one can minimize the number of switches between controllers f_1 and $\bar{f}_2$ necessary to reach the desired neighborhood of the goal. If the stable manifold $\mathcal{W}^s$ matches the zero set of σ and $\mathcal{W}^s$ is made attractive by $\bar{f}_2$ for any point in $\mathcal{Q}_s$ then one gets $\Phi_\infty^{f_1} \circ \Phi_\infty^{\bar{f}_2}(\mathcal{Q}_s) = q^*$, i.e., only 2 steps are necessary to reach the goal. Note however that if the zero set of σ intercepts $\mathcal{W}^c$ more than one time then there exists the possibility that the system will not progress to the goal. In this section we present practical computational heuristic substitutes for σ with zero sets that locally approximate $\mathcal{W}^s$.

1) Divergence: Following the results obtained in Section III-D using the divergence operator seems natural. In the neighborhood of the center manifold if the eigenvalues have all negative real part, then the divergence will be negative, reversing the flow of f_2. If the real part of the eigenvalues are all positive the divergence operator will not reverse the flow. Even in the event of the eigenvalues having simultaneously positive and negative real parts, the sign of the divergence will not change the instability. Define the function $\sigma_1 : \mathcal{Q} \to \mathbb{R}$ by

$$\sigma_1(q) := \mathrm{div}(f_2) = A_R(q)^T.\nabla\varphi(q). \tag{43}$$

2) Maximizing ξ: Another way of escaping $\mathcal{W}^c$ is to follow the direction that maximizes ξ. By definition its maximum is the unity. Let the function $\sigma_2 : \mathcal{Q} \to \mathbb{R}$ be defined by:

$$\sigma_2(q) := \nabla\xi(q)^T f_2(q). \tag{44}$$

Using $L(q) = \xi(q) \geq 0$ as a candidate control Lyapunov function for the system $\dot{q} = \sigma_2(q) f_2(q)$ we observe that

$$\begin{aligned} \dot{L} &= \nabla\xi^T \left(\nabla\xi(q)^T f_2(q)\right) f_2(q) \\ &= \|\nabla\xi(q) f_2(q)\|^2 \geq 0 \end{aligned} \tag{45}$$

The function $\sigma_2(q)$ destabilizes (34) at $\mathcal{W}^c$ if there exists a $\xi^* > 0$ such that the set $\{\dot{L}(\mathcal{C}_{\xi^*} - \mathcal{W}^c) = 0\}$ does not define an invariant manifold (following La Salle's).

3) Stable manifold approximation: The third heuristic computation of σ presented here, aims directly at approximating the stable manifold[10] so to minimize the number of switches between controllers f_1 and $\bar{f}_2$. Suppose there exists a smooth function $G : \mathcal{Q} \to \mathbb{R}$ whose pre-image $G^{-1}[0]$ is $\mathcal{W}^s$. Using the same argumentation as in equations (44) and (45) and replacing ξ by $G(q)^2$ we obtain:

$$\sigma_{3a}(q) := -\nabla(G(q)^2)^T f_2(q). \tag{46}$$

Again, taking $L(q) = G(q)^2 \geq 0$ as a candidate control Lyapunov function we observe that the system $\dot{q} = \sigma_{3a}(q) f_2(q)$ will have its forward limit set in $\mathcal{W}^s$ if $\forall q \in \mathcal{Q} - \mathcal{W}^s$: $\dot{L}(q) = -\|2G(q)\nabla G(q)^T f_2(q)\|^2 \neq 0$. Note that it is possible for the zero set of $\nabla(G(q)^2)^T f_2(q)$ not to be contained in $\mathcal{W}^s$, breaking the desired result. In some cases however, it is possible to use the function

$$\sigma_{3b}(q) := sG(q) \tag{47}$$

where $s \in \{-1, +1\}$. The sign s is chosen so that $\mathcal{W}^c$ can be made unstable, i.e. in a neighborhood of $\mathcal{W}^c$ the signs of $\mathrm{div}(f_2)$ and G should match.

In general, finding an exact approximation of $\mathcal{W}^s$ by an algebraic implicit equation is unattainable since that requires solving a set of partial differential equations [15]. We proceed by finding a k-order polynomial approximation to $\mathcal{W}^s$, denoted by $\widehat{\mathcal{W}}_k^s$. Without loss of generality, we assume that the goal is at the origin, $q^* = 0$, and the tangent of $\mathcal{W}^s$ evaluated at the origin is the span of the first two canonical base vectors[11]. Let

[10] One can observe the difference between Ikeda's proposed algorithm [27] and the one presented here. In his scheme the first step aims only at a specific, one-dimensional trajectory, instead of the entire goal's co-dimension one stable manifold, hence one worries about robustness in the presence of inevitable model error and sensor noise. Moreover, it is not obvious how to integrate perceptual limitations in the resulting control law. In the scheme presented here, we aim at the full co-dimension one stable manifold.

[11] It is always possible to align the tangent of $\mathcal{W}^s$ at the goal with the span of the first two canonical base vectors by means of a translation $p = q - q^*$ and a rotation R. The matrix R is obtained by applying the Gram-Schmidt orthogonalization on the matrix of the eigenvectors of $Df_1(q)|_{q=q^*}$ with eigenvalues sorted by absolute magnitude.

h be the "aligned" version of f_1. We seek to find a function[12] $g : \mathbb{R}^2 \to \mathbb{R}$ such that its graph is $\mathcal{W}^s$, i.e., $x_3 = g(x_1, x_2)$. Define the implicit function G as:

$$G(x_1, x_2, x_3) := g(x_1, x_2) - x_3 \tag{48}$$

Let $\hat{g}_k$ be a k-order polynomial approximation of g at the origin parameterized by $\gamma_{i,j}$:

$$\hat{g}_k(x_1, x_2) = \sum_{\substack{i,j\geq 0 \\ i+j\leq k}} \frac{x_1^i x_2^j}{i!j!}\gamma_{i,j} \tag{49}$$

and let $\hat{h}_k$ be the k-order Taylor expansion of h at the origin:

$$\hat{h}_k(x_1, x_2, x_3) = \sum_{\substack{i,j,l\geq 0 \\ i+j+l\leq k}} \frac{x_1^i x_2^j x_3^l}{i!j!l!}\left(\frac{\partial^i}{\partial x_1^i}\frac{\partial^j}{\partial x_2^j}\frac{\partial^l}{\partial x_3^l}h\right) \tag{50}$$

For the system $\dot{q} = h(q)$ the manifold $G(q) = 0$ is invariant. Therefore for trajectories that start in $G(q) = 0$ we obtain

$$\dot{G}(q) = \nabla G(q)^T h(q) = 0. \tag{51}$$

Replacing g by $\hat{g}_k$, h by $\hat{h}_k$ and x_3 by $\hat{g}_k(x_1, x_2)$ we obtain the following approximation equation:

$$\left(\left[\begin{array}{ccc} \dfrac{\partial \hat{g}_k}{\partial x_1} & \dfrac{\partial \hat{g}_k}{\partial x_2} & -1 \end{array}\right] \cdot \hat{h}_k\right) \circ (x_1, x_2, \hat{g}_k) = 0 \tag{52}$$

Equation (52) is polynomial in $\gamma_{i,j}$ and in x_i. Since by assumption the tangent space of $\mathcal{W}^s$ at the origin is the plane $x_3 = 0$, we immediately obtain:

$$h(0) = \left.\frac{\partial h}{\partial x_1}\right|_{q=0} = \left.\frac{\partial h}{\partial x_2}\right|_{q=0} = 0, \text{ and}$$

$$\gamma_{0,0} = \gamma_{1,0} = \gamma_{0,1} = 0$$

The 2nd order terms of $\gamma_{i,j}$ are obtained by solving the following equation evaluated at the origin, where h_i is the i-th component of h:

$$\left[\begin{array}{c} \gamma_{0,2} \\ \gamma_{1,1} \\ \gamma_{2,0} \end{array}\right] = \left[\begin{array}{ccc} \dfrac{\partial h_2}{\partial x_2} & \dfrac{\partial h_1}{\partial x_2} & 0 \\ \dfrac{\partial h_2}{\partial x_1} & \dfrac{\partial h_1}{\partial x_1} + \dfrac{\partial h_2}{\partial x_2} & \dfrac{\partial h_1}{\partial x_2} \\ 0 & \dfrac{\partial h_2}{\partial x_1} & \dfrac{\partial h_1}{\partial x_1} \end{array}\right]^{-1} \cdot \left[\begin{array}{c} \dfrac{1}{2}\dfrac{\partial^2 h_3}{\partial x_2^2} \\ \dfrac{\partial^2 h_3}{\partial x_1 \partial x_2} \\ \dfrac{1}{2}\dfrac{\partial^2 h_3}{\partial x_1^2} \end{array}\right]$$

Note that a measure of the curvature of $\mathcal{W}^c$ at the origin is given by $\gamma_{1,1}^2 - \gamma_{2,0}\gamma_{0,2}$. The higher order terms of $\gamma_{i,j}$ are obtained recursively by incrementally increasing k in equation (52) and solving for $\gamma_{i,j}$ with $i + j = k$.

F. Illustrative simulations using a norm-like Navigation Function

We now present numerical results of simulations for a norm-like navigation function in order to compare the performance of the functions σ_i defined in Section III-E. Consider the following simply connected configuration space: let $\mathcal{Q} = \{q \in \mathbb{R}^3 : \|q\| \leq 1\}$ and

$$\varphi(q) = x_1^2 + x_2^2 + x_3^2 = \|q\|^2. \tag{53}$$

Clearly, φ is a navigation function in $\mathcal{Q}$ since $\varphi(\partial\mathcal{Q}) = 1$ and φ has a unique minima at the origin. Note that all the level sets of φ are spheres, hence φ_s can be stretched to the boundary of $\mathcal{Q}$ resulting in $\mathcal{R} \equiv \mathcal{Q}$. Below we present the σ_3 function for different approximation levels k. Note that for this particular configuration all the σ_i functions differ from each other.

$$\sigma_3 = \begin{cases} x & \text{if} \quad k = 1 \\ x + \dfrac{y\theta}{2} & \text{if} \quad k = 2 \\ x + \dfrac{y\theta}{2} + \dfrac{y\theta^3}{48} & \text{if} \quad k = 4 \\ x + \dfrac{y\theta}{2} + \dfrac{y\theta^3}{48} + \dfrac{y\theta^5}{480} & \text{if} \quad k = 6 \end{cases}$$

Table I compiles the simulation results. One can conclude, as expected, that the number of iterations of (38) required to reach a fixed neighborhood of the goal dramatically decreases when δ increases. Moreover, although σ_1 and σ_2 do a good job at escaping $\mathcal{W}^c$, they require more iterations in average than the higher order approximation of $\mathcal{W}^s$. The best results, in terms of iteration number, are obtained for σ_3 when $k \geq 2$, where the approximation of $\mathcal{W}^s$ is very good.

TABLE I

SIMULATIONS FOR THE UNICYCLE WITH A NORM TYPE NAVIGATION FUNCTION. EACH ENTRY CORRESPONDS TO THE AVERAGE NUMBER OF SWITCHES "N" FROM A RANDOM INITIAL CONDITION 5 METERS AWAY FROM THE GOAL FOR 50 SIMULATIONS. WE USE THE PARAMETER $\gamma = 10^{-3}$

$\delta =$	0.2		0.5		1	
$\epsilon =$	1 cm	1 mm	1 cm	1 mm	1 cm	1 mm
σ_1	27.9	37.8	9.9	13.2	2.9	3.1
σ_2	29.3	41.0	9.8	12.9	2.7	3.2
$\sigma_3, k = 1$	28.7	38.5	10.3	12.5	2.7	3.0
$\sigma_3, k = 2$	28.2	38.3	9.7	13.5	1.3	1.8
$\sigma_3, k = 4$	29.9	37.8	10.6	13.4	1.3	1.5
$\sigma_3, k = 6$	30.2	37.9	9.2	13.8	1.4	1.5

G. Simulations for a single beacon visual servoing problem

We present here a simulation of a different visual servoing problem: positioning a robot in relation to a single engineered beacon. This problem has been addressed by Kantor [30] and Bhattacharya [31], as discussed in the introduction. Their alternative solution approach can be readily compared to present scheme. Since the visibility set (the complete configuration space) is not a topological sphere, this example also provides a simple illustration of the additional effort required to reason about initial conditions outside the "surround". Figure 4 illustrates how the level sets which are topological spheres (the components of $\mathcal{Q}_s$) form a proper subset of the toroidal visibility set in this case, as illustrated in figure 6(a).

[12] In general this function may not exist outside a neighborhood of the origin

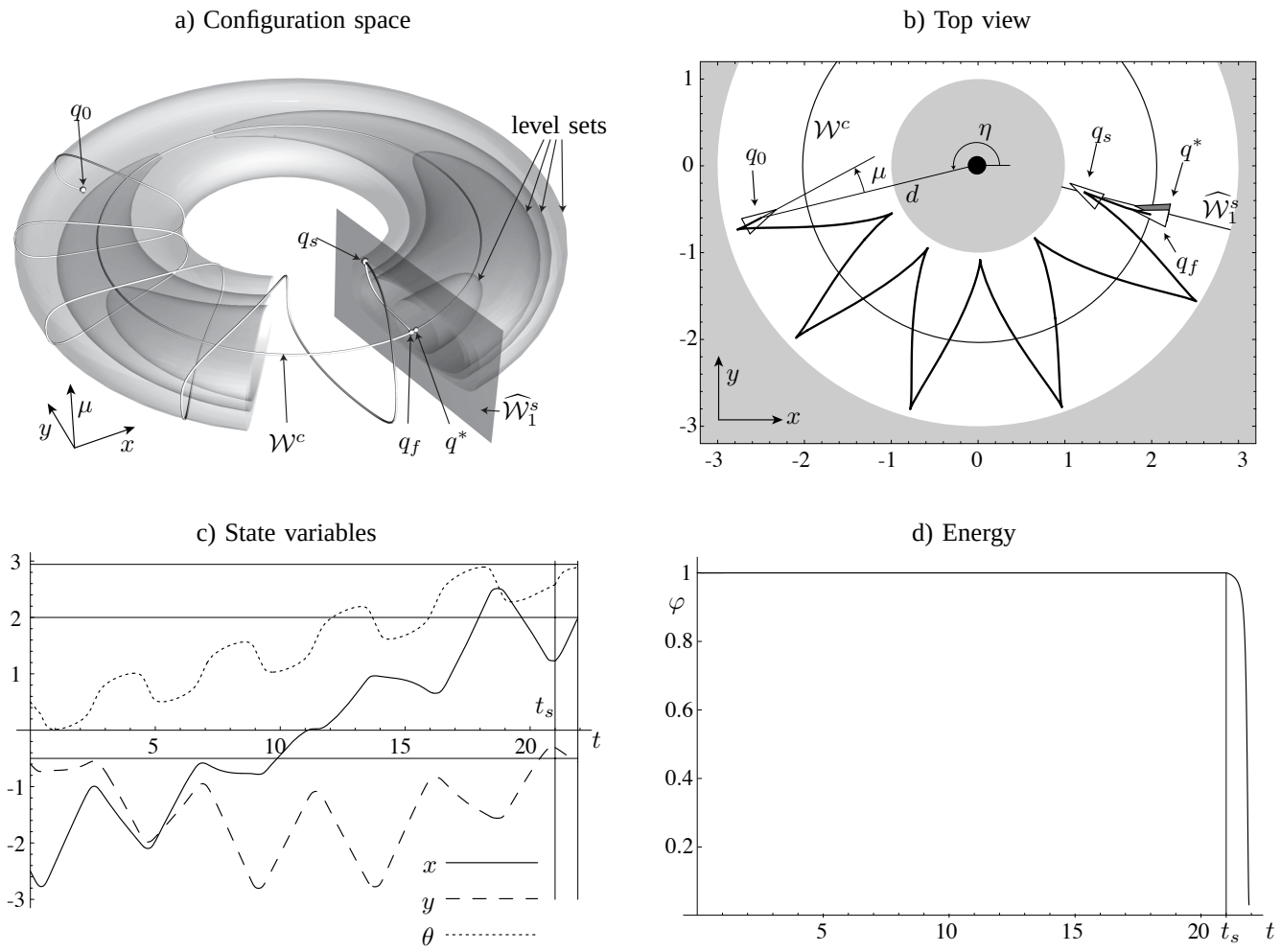

Fig. 6. Simulation of the hybrid controller operating in the visible set of a single beacon landmark described in Section III-G. The initial configuration is q_0, the controller switches at time t_s in position q_s and the final configuration is q_f. **a)** Configuration space plotted on (x, y, μ) for readability purpose. **b)** Top view. The visual beacon is represented by the large black dot. The gray areas violate the visual constraints. **c)** and **d)** State variables and energy plots.

We applied the algorithm developed in this paper to this problem, using again, the unicycle motion model $A = \begin{bmatrix} \cos(\theta) & \sin(\theta) & 0 \end{bmatrix}$. The navigation function is developed in double polar coordinates and it is brought back to $\mathsf{SE}(2)$ by the change of coordinates $c : \mathsf{SE}(2) \to \mathbb{S}^1 \times \mathbb{S}^1 \times \mathbb{R}^+$:

$$\begin{bmatrix} \eta \\ \mu \\ d \end{bmatrix} = c(x, y, \theta) := \begin{bmatrix} \arctan(y/x) \\ \theta - \arctan(y/x) \\ \sqrt{x^2 + y^2} \end{bmatrix} \tag{54}$$

The navigation function reflects the following physical attributes of the sensor:

1) The robot must be in an interval of distances away from the beacon, so to not get too close or too far away from it, specifically $d_m < d < d_M$.
2) The robot's camera must face the beacon at all times, encoded as $\mu_m < \mu < \mu_M$, where μ_m, μ_M are the field of view boundaries of the camera in polar coordinates.

Consider the potential function:

$$\bar{\bar{\varphi}} := \frac{\left(2 - \cos(\eta - \eta^*) - \cos(\mu - \mu^*) + (d - d^*)^2\right)^k}{(1 - \cos(\mu - \mu_m))(1 - \cos(\mu - \mu_M))(d_M - d)(d - d_m)}$$

For the previous potential function we have:

- The goal location in $\mathsf{SE}(2)$, denoted by (x^*, y^*, θ^*), is mapped by c to (η^*, μ^*, d^*). We assume this way that the final orientation of the robot is important.
- The cosine functions are used here, e.g. $(1-\cos(\mu-\mu_m))$, since the state variables η and μ live in $\mathbb{S}^1$. The desired goal is actually $(\eta^* + 2k_1\pi, \mu^* + 2k_2\pi, d^*)$ with $k_1, k_2 \in \mathbb{N}$.
- k is a shaping term.

The resulting navigation function follows the same "squashing" and change of coordinates as in equations (8) and (9). Note that by imposing a minimum distance to the beacon d_m, the configuration space is not simply connected. It is in fact homeomorphic to a solid torus as illustrated in figure 6. This results in $\varphi_s < 1$. Here, some level sets are topological torus and others topological spheres. However, it is observed that the center manifold $\mathcal{W}^c$ is a circle, every level set homeomorphic to the sphere intersects $\mathcal{W}^c$ and every level set homeomorphic to the torus does not intersect $\mathcal{W}^c$. Since for all points in the domain $\mathcal{Q}$ by following the flow of function f_1 have its limit set in $\mathcal{W}^c$ then one can argue that the domain of attraction for the hybrid stabilization algorithm presented here is the entire

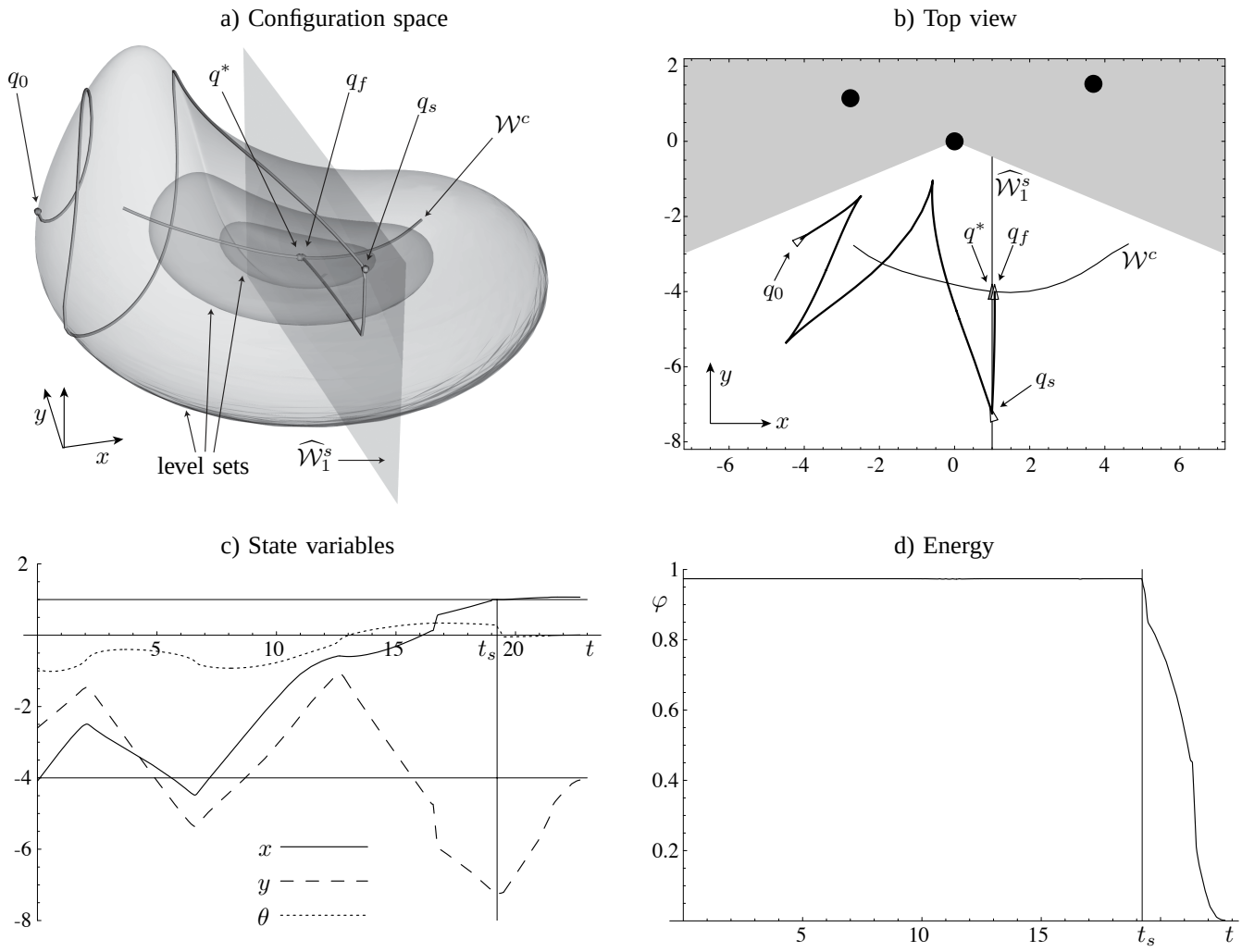

Fig. 7. Simulation of the hybrid controller operating in the visible set of a three beacon landmark. The initial configuration is q_0, the controller switches at time t_s in position q_s and the final configuration is q_f. **a)** Configuration space plotted on $(x, y, 5\theta - 5\arctan(y/x))$ for readability purpose. **b)** Top view. The visual beacons are represented by the large black dots. The gray areas violate the visual constraints. **c)** and **d)** State variables and energy plots.

$\mathcal{Q}$ up to a zero measure set. In fact, experience shows that better trajectories (in the sense of minimum number of "back and forward" parallel parking motion for the vector field f_2) are obtained if the energy level φ is kept very high, i.e., in the torus level sets. There, the trajectories define quasi-periodic orbits that intersect the stable manifold $\mathcal{W}^s$ indefinitely.

For the simulations and experiments we consider the interesting parameters to be the *mean error position* defined by:

$$\text{mean error position} := \text{Mean}_i \left[\|q_f^i - q^*\| \right], \qquad (55)$$

where q_f^i is the final position reached on the ith run; and the *mean arc-length ratio* that gives an idea of how much worse the robot performs against a fully actuated robot that can always follow a straight line to the goal. For continuous time it is defined by:

$$\text{mean arc-length ratio} := \text{Mean}_i \left[\frac{\int_0^{t_f^i} \|q'(q_0^i, t)\| \mathrm{d}t}{\|q_0^i - q^*\|} \right], \qquad (56)$$

where t_f^i is the final time and $q'(q_0^i, t)$ the derivative of the trajectory starting at the initial position q_0^i for the ith run. For the 383 simulations run of a single beacon visual servoing problem we obtained a mean error position of 4.3 cm and a mean arc-length ratio of 4.1. Note that in figure 6 the robot executes a parallel parking maneuver in the plane. Although it is well known that for the unicycle the parallel parking motion is required to move sideways, the trajectory obtained on the plane is a natural consequence of moving on a level set of the navigation function. Moreover, the navigation function enforces that the robot does not hit the obstacles, since doing that would require puncturing the level sets away from the goal.

H. Simulations for the visual servoing problem

A representative numerical simulation for the visual serving problem described in Section II is illustrated in figure 7. Since the navigation function φ, presented in equation (9), is defined in a convex set and has a unique critical point at q^*, all of its level sets are topological spheres. The inputs (40), (41) and (39) are computed using the nonholonomic constraint (12) and the navigation function (9). Table II compiles the simulation results.

IV. Experimental implementation

We now present the results of our implementation of the visual servoing algorithm using the robot RHex [2] in three steps. In Section IV-A, we outline the hardware and software components that comprise the image processing pipeline. It is important to keep in mind that this perceptual apparatus must be quite simple since it is located entirely onboard the robot and runs in real time as we detail below. In Section IV-B we describe the controller implementation, emphasizing the two extensions to the simple version of the algorithm presented above in Section III that compensate for the significant sensor noise and limitations in control authority inherent in this physical setting. We explain why the resulting closed loop (hybrid) behavior is still governed by the correctness results of Section III, notwithstanding these real world adjustments. Finally, we present tables and figures of data summarizing our extensive experimental results for both indoor and outdoor implementations of the complete system.

A. The Perceptual Hardware and Software

The entire visual sensor suite is implemented on a second, dedicated, onboard 300MHz PC104 stack, running Linux, connected by local ethernet to the (QNX based) motor control stack documented in [2]. We implement the following computational pipeline on this second stack at a 10 Hz update rate:

1) Video acquisition: is accomplished by a Sony DFW300 camera via a firewire connection.

2) Image processing library: Early vision is accomplished using our in-house SVision library inspired by Hager's XVision [43] albeit considerably stripped down in comparison.We implement the following image processing methodology:

- color calibration (this step is executed only at startup): A lookup table is used for color classification in the YUV color space (the standard TV NTSC color space) with size $256 \times 256 \times 256$. Different color classes are acquired by selecting different objects in the GUI's camera view. After a color class is acquired its size is increased[13] by a pre-defined amount in the luminance direction of the HLS color space (Hue, Luminance and Saturation) so as to maximize robustness to daylight changes, specifically switching from shade to direct sun exposure.
- blob extraction: the standard 4-neighbor connected components algorithm is used as presented in [44]. A vector of mass, centroid and labeling class is returned per blob found.
- lens correction: the standard Heikkilä [45] lens model is used. The lens correction map includes all the intrinsic camera parameters, including focal length, and returns "normalized" points, with units in meters, projected into a plane 1 meter away from the robot's camera. Calibration is performed at startup using a flat checkerboard surface.

3) Image stabilization: The centroid information provided by the image processing library follows a post-processing roll correction. Since it assumed that the beacons project into a line, following figure 2(a), roll correction is accomplished by fitting a line to the 2D centroid of the 3 blobs (chosen by size and class) and attaching a frame to it. The beacon coordinates are defined in relation to that frame. The following simplified expression is used in the experimental implementation, where (X_i, Y_i) are the centroids of the three beacons in the image plane after Heikkilä's lens correction map:

$$\iota_i = \frac{X_i + \delta Y_i}{1 + \delta^2} \tag{57}$$

$$\zeta_i = \arctan(\iota_i) + \pi/2 \tag{58}$$

with,

$$\delta := \frac{\sum X_i \sum Y_i - 3 \sum X_i Y_i}{(\sum X_i)^2 - 3 \sum X_i^2}, \tag{59}$$

In the simulations developed in Section III-H the robot is assumed to live in the plane. Therefore, no obstacles relating to pitch are encoded in the navigation function. However, in the experimental implementation there can be large disturbances that pitch the robot enough for the beacons to leave the field of view either from the bottom or from the top of the image. We coded a state machine that in case of "emergency" will stop and rotate the robot in place until it relocates the beacons. This simple procedure corrected for all the temporary failures that occurred due to excessive pitching.

4) Supervisory state machine: The transitions between the controllers f_1 and $\bar{f}_2$ are implemented using a standard state machine formulation. The robot is initiated with controller $\bar{f}_2$. A transition occurs if the robot crosses the stable manifold approximation switching to controller f_1. If f_1 fails to bring the robot to a pre-defined neighborhood of the goal location, i.e. reaches the center manifold outside the goal's neighborhood and a fixed amount of time as passed, then another transition occurs, switching back to controller $\bar{f}_2$. The robot stops when it reaches the goal's neighborhood. As mentioned before, the state machine will also deal with particular emergency situations.

B. Controller Implementation.

The control algorithms use the camera map exactly as defined above in Section II. However the substantial perceptual noise and limitations in control authority associated with our physical RHex environment require two additional complications in the controller implementation.

First, although the horizontal plane behavior of the robot RHex is reasonably well approximated by the unicycle mechanics presented in Section II-C, the limited number of gaits available for any given terrain [46] typically dictate that the available fore-aft speed control be limited to a few discrete velocity magnitudes. Thus, a more accurate model of control authority would replace u_1 in equation (11) with a variable taking its values in a discrete set. Fortunately, gradient vector fields can be scaled in an arbitrary (albeit sign definite) manner with no change in steady state behavior. Namely, for any gradient field, $f(x) = -\nabla\varphi$ and any positive scalar valued function, $\sigma(x)$, observe that φ remains a Lyapunov function for the scaled field $\sigma(x)f(x)$. Our implementation using a

[13]The color's acquired simply-connected volume is projected into the Hue and Saturation plane and then spread over an interval in the Luminance axis.

discrete magnitude field can now be modeled by $\sigma(x) := \sigma_0/||f(x)||$.

Second, in systems where noise is introduced via imperfect perception or actuation the vector field f_2 loses its φ-invariance. Although a thorough-going treatment of the stochastic version of our problem lies well beyond the scope of this paper, the reliance on gradient vector fields once again affords an intuitively simple "regulator" against these undesirable (and, ultimately, dangerous) fluctuations in proximity to the obstacles. Namely, suppose that the noise is additive and zero mean. Rewrite equation (34) as:

$$\dot{q} = \bar{f}_2(q) + v(t) \tag{60}$$

Define the new input $\hat{f}_2$ as:

$$\begin{aligned} \hat{f}_2 &:= \bar{f}_2(q) + \beta\left(\varphi^* - \varphi(q)\right) f_1(q) \\ &= \sigma J(A) \nabla\varphi + \beta\left(\varphi^* - \varphi\right) H \nabla\varphi, \end{aligned} \tag{61}$$

where β is a positive scalar and φ^* is the desired *target level set*, normally chosen to be slightly less then 1. The dynamics of φ for $\dot{q} = \hat{f}_2(q) + v(t)$ are:

$$\begin{aligned} \dot{\varphi} &= \underbrace{\nabla\varphi^T \bar{f}_2}_{=0} + \beta(\varphi^* - \varphi) \underbrace{\nabla\varphi^T H \nabla\varphi}_{\gamma} + \underbrace{\nabla\varphi^T v}_{w} \\ &= \beta\gamma(\varphi^* - \varphi) + w \end{aligned} \tag{62}$$

As $q(t)$ evolves over time, $\varphi(q(t))$ converges to a neighborhood of φ^* if $\gamma > 0$ and w is small in proportion. In practice this means that the robot will stay in the proximity of the target level set φ^* while it is in motion, escaping the center manifold. The experiments performed on RHex, described next, revealed that adding the second term to the vector field (61) is indeed necessary. The robot was not able at all to follow a particular level set when $\bar{f}_2$ was solely used. In contrast, note that f_1 is energy dissipative, hence standard arguments from Lyapunov theory establish its robustness against these sorts of perturbations without the requirement of any further modification.[14] Although formal robustness analysis is generally not available for nonlinear systems, the nondegenerate gradient systems of the kind introduced in this paper are structurally stable, hence "small" perturbations away from the nominal model are guaranteed to result in only "small" perturbations in the limit set.

The resulting modified input of (41) used in the experiments, before applying the scaling required for RHex's discrete actuation presented in the beginning of this section, is:

$$u_p := B^\dagger \left[\sigma J(A) + \beta\left(\varphi^* - \varphi\right) I\right] \nabla\varphi \tag{63}$$

As a final note we would like to remind the reader that throughout the paper we consider only the problem of point stabilization and avoid the tracking problem. In the experimental implementation the robot eventually "tracks" a level set of the navigation function but still does not track any particular fixed trajectory. Tracking changes completely the structure of the problem since in general time-invariant vector fields can no longer be used for control.

[14]Specifically, the Lie derivative of φ along $\hat{f}_1 := f_1 + v$ is "usually" negative — except possibly in a small neighborhood of the center manifold whose size is regulated by the relative magnitude of f_1 and the variance of v. It follows that this neighborhood remains an attractor "on average".

C. Experimental results

The first data set, a trace of the visually perceived pose and energy level resulting from application of controller f_2, illustrated in figure 8, gives a feeling for the robustness of these gradient style controllers as the robot roughly but reliably traces out the desired trajectory in the face of notable sensor noise, the inevitable perturbations from uneven ground, as well as the very severe parametric uncertainty arising from the crudeness of the unicycle model as a description of the horizontal plane behavior of RHex. Far away from the beacons the pose estimation performs poorly, as seen in the high variance of the data. This experiment is conducted outdoors using RHex's onboard camera only, according to the procedure documented above in Section IV-A, for two different target levels, as defined before equation (62).

The second data set — a graphical and tabular summary of convergence from several different initial configurations — portrays the nature of "practical stability" [25] assuring convergence to a small neighborhood of the goal pose with the guarantee of maintaining visibility (never losing sight of the triple-beacon landmark) along the way. This experiment was conducted indoors with the ground truth data acquired by an overhead camera running at 30Hz. Quantitatively, the interesting parameter to measure is the *mean arc-length ratio* of the path, defined in discrete time by:

$$\text{mean arc-length ratio} := \text{Mean}_i \left[\frac{\sum_k \|q_k^i - q_{k-1}^i\|}{\|q_0^i - q^*\|} \right], \tag{64}$$

where k spans the indexes of the samples for the ith experiment. Table II compiles the experimental results and figure 9 illustrates three representative runs. No chattering effect was observed in both the experiments. This is due to the state machine formulation (that prevent f_1 and $\bar{f}_2$ to switch in an "incoherent" fashion) and RHex's actuation model, realizing discrete steps. Note however that in wheeled vehicles chattering may occur when controller $\bar{f}_2$ is used very close to the goal, i.e. with a very small energy. Since $\bar{f}_2$ will live on a very small level set of the navigation function, this results in very small oscillations around the goal.

TABLE II

EXPERIMENTS EXECUTED USING THE ROBOT RHEX IN COMPARISON TO SIMULATIONS OF A UNICYCLE ON THE SIMPLY CONNECTED CONFIGURATION SPACE DEFINED IN EQUATION (10)

	#	mean error position	mean arc-length ratio
Simulations:	368	5.3 cm	2.9
Experiments: 1	5	17.6 cm	9.3
2	5	17.8 cm	6.2
3	5	17.6 cm	6.5
4	5	26.1 cm	5.2
5	5	11.5 cm	5.5
6	5	27.9 cm	4.9

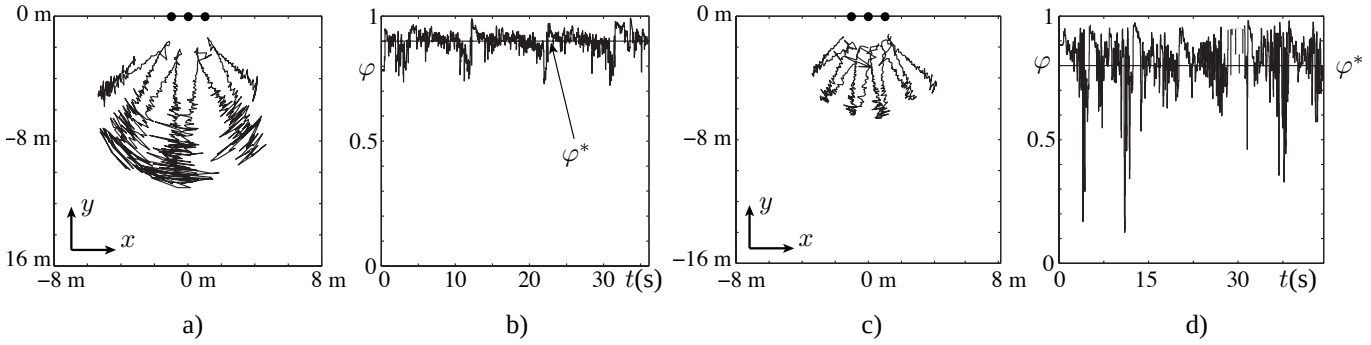

Fig. 8. RHex's outdoor experiments on packed dirt for controller f_2. **a)** Top view of perceived trajectory with units in meters and **b)** perceived energy $\varphi(q)$ for target level $\varphi^* = 0.9$. **c)** Top view of perceived trajectory and **d)** perceived energy $\varphi(q)$ for target level $\varphi^* = 0.8$. The beacons are represented by the black dots.

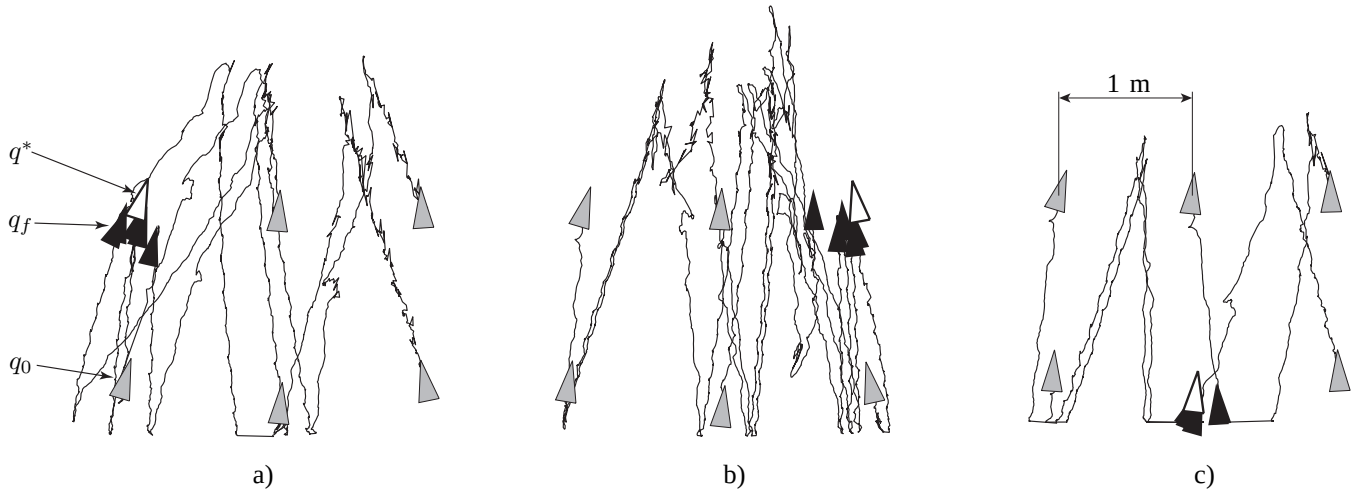

Fig. 9. RHex's ground truth measurement experiments. Different goal locations q^* are represented by the thick line white triangles. The initial configurations q_0 are represented by the thin line gray triangles and the final configurations q_f by the solid black triangles.

V. Conclusions and future directions

We present a robust visual servo suitable for registering a legged robot with limited perception relative to engineered landmarks over rugged outdoor terrain. At the heart of our algorithm is a provably correct hybrid controller that reuses navigation functions developed for fully actuated bodies on kinematically constrained systems. It is straightforward to extend the guarantee of obstacle avoidance. Verifiable assumptions are given for convergence to an arbitrarily small neighborhood of the goal. We present various simulations for different perceptual models and summarize the results of an extensive empirical implementation on the legged robot RHex. We are presently exploring generalizations to robots with higher degrees of freedom and alternative motion constraints as well as a variety of alternative landmark schemes.

VI. Acknowledgments

We thank John Guckenheimer for several useful conversations related to the computation of invariant manifolds and George Kantor, Al Rizzi and Anthony Bloch for a number of stimulating and helpful conversations bearing on the problem addressed in this paper. We would like to thank the reviewers for a number of very helpful suggestions and comments regarding the presentation of this material.

Appendix I
Camera maps

Define $c^{bc} : \mathsf{SE}(2) \to \mathcal{C}$ as the map from local body coordinates to the intermediate space $\mathcal{C}$ by:

$$c^{bc}(x_b, y_b, \theta_b) := \begin{bmatrix} \arctan(-x_b/y_b) \\ \theta_b - \arctan(-x_b/y_b) \\ \sqrt{x_b^2 + y_b^2} \end{bmatrix}$$

with inverse:

$$(c^{bc})^{-1}(\phi, \psi, r) := \begin{bmatrix} -r\sin(\phi) \\ r\cos(\phi) \\ \phi + \psi \end{bmatrix}$$

Define $c^{wb} : \mathsf{SE}(2) \to \mathsf{SE}(2)$ as the map from world coordinates to body coordinates:

$$c^{wb}(x_w, y_w, \theta_w) := -\begin{bmatrix} R_{\theta_w}^T & \mathbf{0} \\ \mathbf{0} & 1 \end{bmatrix} \begin{bmatrix} x_w \\ y_w \\ \theta_w \end{bmatrix}$$

with equal inverse since c^{wb} is an involution.

APPENDIX II
COMPUTATION OF INVERSE CAMERA MAP

Let $Y_i = \left[\begin{array}{cc} \cos(\zeta_i) & \sin(\zeta_i) \end{array} \right]$ where ζ_i are the angles defined in Section II-A. Knowing that $Y^T J Y = 0$ we have:

$$Y_i^T J R_\phi (\rho_i R_{\alpha_i} R_\psi + rI)\hat{e}_2 = 0 \tag{65}$$

in particular, since $\alpha_1 = -\alpha_3 = \alpha;\ \rho_2 = 0$

$$rY_2^T J R_\phi \hat{e}_2 = 0 \Leftrightarrow R_\phi = \delta_1 \left[\begin{array}{cc} JY_2 & -Y_2 \end{array} \right] \tag{66}$$

The constant $\delta_1 = \pm 1$ is chosen so that $-\frac{\pi}{2} < \phi < \frac{\pi}{2}$ resulting in:

$$\phi = \zeta_2 + \frac{\pi}{2} \tag{67}$$

Let Y' and Y be obtained by expressions (5) and (6). Then:

$$\begin{array}{rl} & \rho_i Y_i^T R_{\alpha_i} J R_\psi R_\phi \hat{e}_2 + r Y_i^T J R_\phi \hat{e}_2 = 0 \\ \Leftrightarrow & \left[\begin{array}{cc} Y'^T & Y^T \end{array} \right] \left[\begin{array}{c} J R_\phi R_\psi \hat{e}_2 \\ r J R_\phi \hat{e}_2 \end{array} \right] = 0 \end{array} \tag{68}$$

Let $Y_\perp^T$ be the orthogonal complement of the subspace generated by the lines of $Y^\dagger$, i.e. $Y_\perp$ lives in the null space of $Y^\dagger$, with $Y^\dagger = (YY^T)^{-1}Y$ the pseudo-inverse of Y^T. Since $\left[\begin{array}{cc} Y^{\dagger T} & Y_\perp \end{array} \right]$ is full rank then the previous expression is equivalent to:

$$\begin{array}{rl} & \left[\begin{array}{c} Y^\dagger \\ Y_\perp^T \end{array} \right] \left[\begin{array}{cc} Y'^T & Y^T \end{array} \right] \left[\begin{array}{c} J R_\phi R_\psi \hat{e}_2 \\ r J R_\phi \hat{e}_2 \end{array} \right] = 0 \\ \Leftrightarrow & \left[\begin{array}{cc} Y^\dagger Y'^T & I \\ Y_\perp^T Y'^T & 0 \end{array} \right] \left[\begin{array}{c} J R_\phi R_\psi \hat{e}_2 \\ r J R_\phi \hat{e}_2 \end{array} \right] = 0 \end{array} \tag{69}$$

Solving for R_ψ we get:

$$x = \delta_2 \frac{Y' Y_\perp}{\|Y' Y_\perp\|} \tag{70}$$

$$R_\psi = R_\phi^T \left[\begin{array}{cc} Jx & -x \end{array} \right] \tag{71}$$

Simplifying we obtain ψ:

$$\psi = \arctan(\delta_2 R_\phi^T J Y' Y_\perp) \tag{72}$$

Again $\delta_2 = \pm 1$ is chosen so that $-\frac{\pi}{2} < \psi < \frac{\pi}{2}$. Finally solving for r in (69) we get:

$$\begin{array}{rl} & Y^\dagger Y'^T J \left[\begin{array}{cc} Jx & -x \end{array} \right] \hat{e}_2 + r J R_\phi \hat{e}_2 = 0 \\ \Leftrightarrow & r \|J R_\phi \hat{e}_2\| = \|Y^\dagger Y'^T J \left[\begin{array}{cc} Jx & -x \end{array} \right] \hat{e}_2\| \\ \Leftrightarrow & r = \dfrac{\|Y^\dagger Y'^T J Y' Y_\perp\|}{\|Y' Y_\perp\|} \end{array} \tag{73}$$

APPENDIX III
FENICHEL'S SINGULAR PERTURBATION THEOREM

Theorem 4 (Fenichel [47]): Consider the system (28) with $0 \leq \alpha \ll 1$. Suppose that for $\alpha = 0$, (28) admits an equilibrium manifold of dimension m, $0 < m < n$, denoted by $\mathcal{W}_h^0$ and for all $q^* \in \mathcal{W}_h^0$, the Jacobian matrix, $D_q h_\alpha|_{(q^*,0)}$ admits $n - m$ eigenvalues with a strictly negative real part. Then, for every open and bounded subset Ω_0 of $\mathcal{W}_h^0$, there exists an open neighborhood V_0 of Ω_0 in $\mathbb{R}^n$, such that, for α positive and small enough, the perturbed system (28) admits an attractive invariant sub-manifold $\mathcal{W}_h^\alpha$ contained in V_0 and close to $\mathcal{W}_h^0$.

The previous theorem establish that under appropriate conditions the "slow" dynamics of h_α, defined in equation (27) , approaches the center manifold of h_0 as α goes to zero. For a tutorial treatment of Singular Perturbations please see [48] or [49].

APPENDIX IV
FEČKAN'S EXTENSION OF THE BENDIXSON'S CRITERIA

Definition 2 (Fečkan [39]): Let $M \subset \mathbb{R}^l$ be an m-dimensional compact smooth orientable submanifold with a nonempty border ∂M. Hence ∂M is an $m-1$-dimensional compact smooth orientable sub-manifold. Assume that $m \geq 2$. Let $V \subset \mathbb{R}^n$ be a k-dimensional smooth submanifold of $\mathbb{R}^n$ with empty border $\partial V = \emptyset$. Let $\beta \in \mathrm{Lip}(\partial M, \mathbb{R}^n)$ be such that $\beta(M) \subset V$ and $\tau = \beta / \partial M$ satisfy:

I τ is injective on ∂M.
II The inverse $\tau^{-1} : \tau(\partial M) \to \mathbb{R}^l$ is Lipschitz on the set $\tau(\partial M) \subset \mathbb{R}^n$.

We call the set $S = \tau(\partial M)$ an $m-1$-V-*L-boundary* of V. It is a generalization of smooth submanifolds of V.

Theorem 5 (Fečkan [39]): Let $g_1, g_2, \cdots, g_p \in C^2(\mathbb{R}^n, \mathbb{R})$ be first integral of (22). If $V = G^{-1}[0]$ is a nondegenerate level set of the mapping $G = (g_1, g_2, \cdots, g_p)$ and in addition $\mathrm{div} f_2 \neq 0$ on V, then there is no $n-p-1$-V-L-boundary S of V which is invariant for (22).

REFERENCES

[1] Koditschek, D., "The control of natural motion in mechanical systems." *ASME Journal of Dynamic Systems, Measurement, and Control*, vol. 113, no. 4, pp. 547–551, Dec 1991.

[2] Saranli, U. and Buehler, M. and Koditschek, D., "Rhex: A simple and highly mobile hexapod robot," *The International Journal of Robotics Research*, vol. 20, no. 7, pp. 616–631, 2001.

[3] Lopes, G. and Koditschek, D., *Navigation Functions for Dynamical, Nonholonomically Constrained Mechanical Systems*. Springer, 2006, ch. I, pp. 135–155.

[4] Zhang, H. and Ostrowski, J., "Visual servoing with dynamics: Control of an unmanned blimp," in *Proc. of International Conference on Robotics and Automation*, 1999.

[5] Malis, E. and Chaumette, F. and Boudet, S., "2-1/2-d visual servoing," *IEEE Transactions on Robotics and Automation*, pp. 238–250, 1999.

[6] Mezouar, Y. and Chaumette, F., "Avoiding self-occlusions and preserving visibility by path planning in the image," *Robotics and Autonomous Systems*, vol. 41, pp. 77–87, 2002.

[7] Comport, A. and Marchand, E. and Chaumette, F., "Robust model-based tracking for robot vision," in *Proc. of IEEE/RSJ International Conference on intelligent Robots and Systems*, Sendai, Japan, 2004, pp. 692–697.

[8] Wunsch, P. and Hirzinger, G., "Real-time visual tracking of 3-d objects with dynamic handling of occlusion," in *Proc. of IEEE International Conference on Robotics and Automation*, Albuquerque, New Mexico, 1997, pp. 2868–2873.

[9] Chesi, G. and Hashimoto, K. and Prattichizzo, D. and Vicino, A., "Keeping features in the field of view in eye-in-hand visual servoing: A switching approach," *IEEE Transactions on Robotics*, vol. 20, no. 5, pp. 908–913, 2004.

[10] Cowan, N. and Weingarten, J. and Koditschek, D., "Visual servoing via navigation functions," *Transactions on Robotics and Automation*, vol. 18, no. 4, pp. 521–533, August 2002.

[11] Chen, J. and Dawson, D. and Dixon, W. and Chitrakaran, V., "Navigation function based visual servo control," in *Proc. of American Control Conference*, 2005, pp. 3682–3687.

[12] Koditschek, D. and Rimon, E., "Robot navigation functions on manifolds with boundary," *Advances in Applied Mathematics*, vol. 11, pp. 412–442, 1990.

[13] Mansard, N. and Chaumette, F., "Visual servoing sequencing able to avoid obstacles," in *Proc. of IEEE International Conference on Robotics and Automation*, April 2005.

[14] Brockett, R., *Asymptotic stability and feedback stabilization*, ser. Differential Geometric Control Theory. Birkhauser, Boston: R. W. Brockett, R. S. Millman, and H. J. Sussmann, 1983, pp. 181–191.

[15] Guckenheimer, J. and Holmes, P., *Nonlinear Oscillations, Dynamical Systems, and Bifurcations of Vector Fields*. Verlag, New York, 1983.

[16] Khennouf, H. and Wit, C., "On the construction of stabilizing discontinuous controllers for nonholonomic systems," in *Proc. of IFAC Nonlinear Control Systems Design Symposium*, Tahoe City, USA, 1995, pp. 747–752.

[17] Luo, J. and Tsiotras, P., "Exponentially convergent control laws for nonholonomic systems in power form," *Systems and Control Letters*, vol. 35, pp. 87–95, 1998.

[18] Astolfi, A., "Discontinuous control of nonholonomic systems," *Systems and Control Letters*, vol. 27, pp. 37–45, 1996.

[19] Tayebi, A. and Tadjine, M. and Rachid, A., "Discontinuous control design for the stabilization of nonholonomic systems in chained form using the backstepping approach," in *Proc. of IEEE Conference on Decision and Control*, 1997, pp. 3089–3090.

[20] Monaco, S. and N, D.-Cyrot, "An introduction to motion planning using multirate digital control," in *Proc. of IEEE Conference on Decision and Control*, 1992, pp. 1780–1785.

[21] Sordalen, O. and Egeland, O., "Exponential stabilization of nonholonomic chained systems," *IEEE Trans. Automation and Control*, vol. 40, no. 1, pp. 35–49, 1995.

[22] Pomet, J., "Explicit design of time-varying stabilizing control laws for a class of controllable systems without drift," *Systems and Control Letters*, vol. 18, pp. 147–158, 1992.

[23] Samson, C., "Control of chained systems - application to path following and time-varying point stabilization of mobile robots," *IEEE Trans. Automation and Control*, vol. 40, no. 1, pp. 64–77, 1995.

[24] Gans, N., "Hybrid Switched System Visual Servo Control", Ph.D., University of Illinois Urbana-Champaign, 2005

[25] Morin, P. and Samson, C., "Practical stabilization of driftless systems on Lie groups: The transverse function approach," *IEEE Transactions on Automatic Control*, vol. 48, no. 9, pp. 1496–1508, September 2003.

[26] Bloch, A. and Reyhanoglu, M., "Control and stabilization of nonholonomic dynamic systems," *IEEE Transactions on Automatic Control*, vol. 37, no. 11, November 1992.

[27] Ikeda, T. and Mita, T. and Anderson, B., "Variable constraint control for a class of nonholonomic systems," Department of Mechanical Control and Systems, Tokyo Institute of Technology, Tech. Rep., 2003.

[28] Murrieri, P. and Fontanelli, D. and Bicchi, A., "A hybrid-control approach to the parking problem of a wheeled vehicle using limited view-angle visual feedback," *International Journal of Robotics Research*, vol. 23, no. 4-5, pp. 437–448, April-May 2004.

[29] Folio, D. and Cadenat, V., "A controller to avoid both occlusions and obstacles during a vision-based navigation task in a cluttered environment," in *Proc. of 44th IEEE Conference on Decision and Control*, December 2005.

[30] Kantor, G. and Rizzi, A., "Sequential composition for control of underactuated systems," Robotics Institute, Carnegie Mellon, Tech. Rep. CMU-RI-TR-03-23, 2003.

[31] Bhattacharya, S. and Murrieta-Cid, R. and Hutchinson, S., "Path planning for a differential drive robot: Minimal length paths-a geometric approach," in *Proc. of IEEE/RSJ International Conference on Intelligent Robotics and Systems*, 2004, pp. 2793–2798.

[32] Burridge, R. and Rizzi, A. and Koditschek, D., "Sequential composition of dynamically dexterous robot behaviors," *The International Journal of Robotics Research*, vol. 18, no. 6, pp. 534–555, June 1999.

[33] Lopes, G. and Koditschek, D., "Visual registration and navigation using planar features," in *Proc. of IEEE International Conference in Robotics and Automation*, Taipei, Taiwan, 2003.

[34] Koditschek, D., "The application of total energy as a Lyapunov function for mechanical control systems," in *Dynamics and control of multibody systems (Brunswick, ME, 1988)*. Providence, RI: Amer. Math. Soc., 1989, pp. 131–157.

[35] Rimon, E. and Koditschek, D., "Exact robot navigation using artificial potential function," *IEEE Transactions on Robotics and Automation*, vol. 8, no. 5, October 1992.

[36] Zenkov, D. and Bloch, A. and Marsden, J., "The Lyapunov-Malkin theorem and stabilization of the unicycle with rider," *Systems and Control Letters*, vol. 46, pp. 293–302, 2002.

[37] Lopes, G. and Koditschek, D., "Level sets and stable manifold approximations for perceptually driven nonholonomically constrained navigation," in *Proc. of IEEE/RSJ International Conference on Intelligent Robots and Systems*, Sendai, Japan, 2004.

[38] Arnold, V., *Ordinary differential equations*. The MIT press, 1973.

[39] Fečkan, M., "A generalization of Bendixson's criterion," in *Proc. of the American Mathematical Society*, vol. 129, no. 11, 2001, pp. 3395–3399.

[40] Fečkan, M., "Criteria on the nonexistence of invariant Lipschitz submanifolds for dynamical systems," *Journal of Differential Equations*, no. 174, pp. 392–419, 2001.

[41] Li, M., "Dynamics of differential equations on invariant manifolds," *Journal of Differential Equations*, no. 168, pp. 295–320, 200.

[42] Giraldo, L. and Gascón, F., "New proof and generalizations of the Demidowitsch-Schneider criterion," *Journal of Mathematical Physics*, vol. 41, no. 9, 2000.

[43] Hager, G. and Toyama, K., "Xvision: A portable substrate for real-time vision applications," *Computer Vision and Image Understanding*, vol. 69, no. 1, pp. 023–037, 1998.

[44] Ballard, D. and Brown, C., *Computer Vision*. Prentice-Hall, 1982.

[45] Heikkilä, J. and Silven, O., "A four-step camera calibration procedure with implicit image correction," in *Proc. of IEEE Conference on Computer Vision and Pattern Recognition*, 1997, p. 1106.

[46] Weingarten, J. and Lopes, G. and Buehler, M. and Groff, D. and Koditschek, D., "Automated gait adaptation for legged robots," in *Proc. of IEEE International Conference on Robotics and Automation*, vol. 3, 2004, pp. 2153–2158.

[47] Fenichel, N., "Geometric singular perturbation theory for ordinary differential equations," *Journal of Differential Equations*, vol. 31, pp. 53–98, 1979.

[48] Wiggins, S., *Normally hyperbolic invariant manifolds in dynamical systems*. Springer-Verlag, 1994.

[49] Khalil, H., *Nonlinear Systems*. Prentice Hall, 1996.